the FEBS Journal

Human Δ^3,Δ^2-enoyl-CoA isomerase, type 2: a structural enzymology study on the catalytic role of its ACBP domain and helix-10

Goodluck U. Onwukwe[1], Petri Kursula[1,2], M. Kristian Koski[1], Werner Schmitz[3] and Rik K. Wierenga[1]

1 Biocenter Oulu and Faculty of Biochemistry and Molecular Medicine, University of Oulu, Finland
2 Department of Biomedicine, University of Bergen, Norway
3 Theodor Boveri Institute of Biosciences (Biocenter), University of Würzburg, Germany

Keywords
crotonase; ECI; helix-10; oxyanion hole; SAXS

Correspondence
R. K. Wierenga, PO Box 5400, University of Oulu, FI-90014 Oulu, Finland
Fax: +358 8 344 064
Tel: +358 2 94481199
E-mail: rik.wierenga@oulu.fi

(Received 24 September 2014, revised 10 December 2014, accepted 12 December 2014)

doi:10.1111/febs.13179

The catalytic domain of the trimeric human Δ^3,Δ^2-enoyl-CoA isomerase, type 2 (HsECI2), has the typical crotonase fold. In the active site of this fold two main chain NH groups form an oxyanion hole for binding the thioester oxygen of the 3E- or 3Z-enoyl-CoA substrate molecules. A catalytic glutamate is essential for the proton transfer between the substrate C2 and C4 atoms for forming the product 2E-enoyl-CoA, which is a key intermediate in the β-oxidation pathway. The active site is covered by the C-terminal helix-10. In HsECI2, the isomerase domain is extended at its N terminus by an acyl-CoA binding protein (ACBP) domain. Small angle X-ray scattering analysis of HsECI2 shows that the ACBP domain protrudes out of the central isomerase trimer. X-ray crystallography of the isomerase domain trimer identifies the active site geometry. A tunnel, shaped by loop-2 and extending from the catalytic site to bulk solvent, suggests a likely mode of binding of the fatty acyl chains. Calorimetry data show that the separately expressed ACBP and isomerase domains bind tightly to fatty acyl-CoA molecules. The truncated isomerase variant (without ACBP domain) has significant enoyl-CoA isomerase activity; however, the full-length isomerase is more efficient. Structural enzymological studies of helix-10 variants show the importance of this helix for efficient catalysis. Its hydrophobic side chains, together with residues from loop-2 and loop-4, complete a hydrophobic cluster that covers the active site, thereby fixing the thioester moiety in a mode of binding competent for efficient catalysis.

Database
Structural data are available in the PDB database under the accession numbers 4U18 (ISO-ECI2), 4U19 (ISOA-ECI2), 4U1A (ISOB-ECI2)

Abbreviations
ACBP, acyl-CoA binding protein; ACBP-ECI2, the ACBP domain of HsECI2; DECI, dienoyl-CoA isomerase (mitochondrial and peroxisomal); DmMFE2, the *Drosophila melanogaster* MFE2; ECH, enoyl-CoA hydratase-1 (mitochondrial); ECI1, Δ^3,Δ^2-enoyl-CoA isomerase type 1 (mitochondrial); ECI2, Δ^3,Δ^2-enoyl-CoA isomerase, type 2 (mitochondrial and peroxisomal); ECI, Δ^3,Δ^2-enoyl-CoA isomerase; FL-ECI2, the full-length variant of HsECI2; HsECI2, the human ECI2; ISOA-ECI2, the V349A variant of ISO-ECI2; ISOB-ECI2, the (Δ350-355) variant of ISO-ECI2; ISO-ECI2, the isomerase domain variant of HsECI2; ITC, isothermal titration calorimetry; MFE1, multifunctional enzyme type 1 (peroxisomal); MFE2, multifunctional enzyme type 2 (peroxisomal); OAH, oxyanion hole; SAXS, small angle X-ray scattering; SCP2, sterol carrier protein type 2; SGC, Structural Genomics Consortium; SLS, static light scattering.

Introduction

Δ^3,Δ^2-enoyl-CoA isomerases (ECIs) catalyze an important reaction which allows unsaturated fatty acids with Z/E double bonds (also known as *cis*/*trans* double bonds) at odd positions, like oleic acid (Z9-octadecenoic acid) and linoleic acid (Z9,Z12-octadecadienoic acid) [1], to enter the classical β-oxidation pathway for the degradation of fatty acids (Fig. 1). A key intermediate of the latter pathway is 2E-enoyl-CoA. ECI (EC 5.3.3.8) catalyses the conversion of 3Z-enoyl-CoA and 3E-enoyl-CoA substrates to 2E-enoyl-CoA (Fig. 1). Other enzymes involved in this auxiliary pathway are $\Delta^{3,5}\Delta^{2,4}$-dienoyl-CoA isomerase (DECI) and 2,4-dienoyl-CoA reductase [1,2]. This is an important pathway, and several studies have reported on disease symptoms related to enzyme deficiencies of mitochondrial 2,4-dienoyl-CoA reductase [3] and mitochondrial ECI [4]. To the best of our knowledge, in the yeast *Saccharomyces cerevisiae* there is only one ECI [5], whereas in mammals there are several isoenzymes, located in both the peroxisomes and mitochondria. The mammalian ECI type 1 (ECI1) is located only in mitochondria. The mammalian ECI type 2 (ECI2) is located in peroxisomes as well as in mitochondria. Therefore, in mammals, there are at least two isomerases in mitochondria (ECI1 and ECI2). Also in peroxisomes there are two isomerases: ECI2 and the multifunctional enzyme type 1 (MFE1). It is not understood why mammals have several isomerase isozymes. The kinetic properties of each of these isomerases from rat have been reported, showing a broad range of fatty acyl chain length specificities and different kinetic parameters for 3Z- and 3E-enoyl-CoA substrates [6]. Rodents possess a third mitochondrial ECI, which has been identified recently and which is homologous to ECI2 [7]. Structures have been described for ECI1 from rat mitochondria (1XX4) [8] and human mitochondria (1SG4) [9], MFE1 from rat peroxisomes

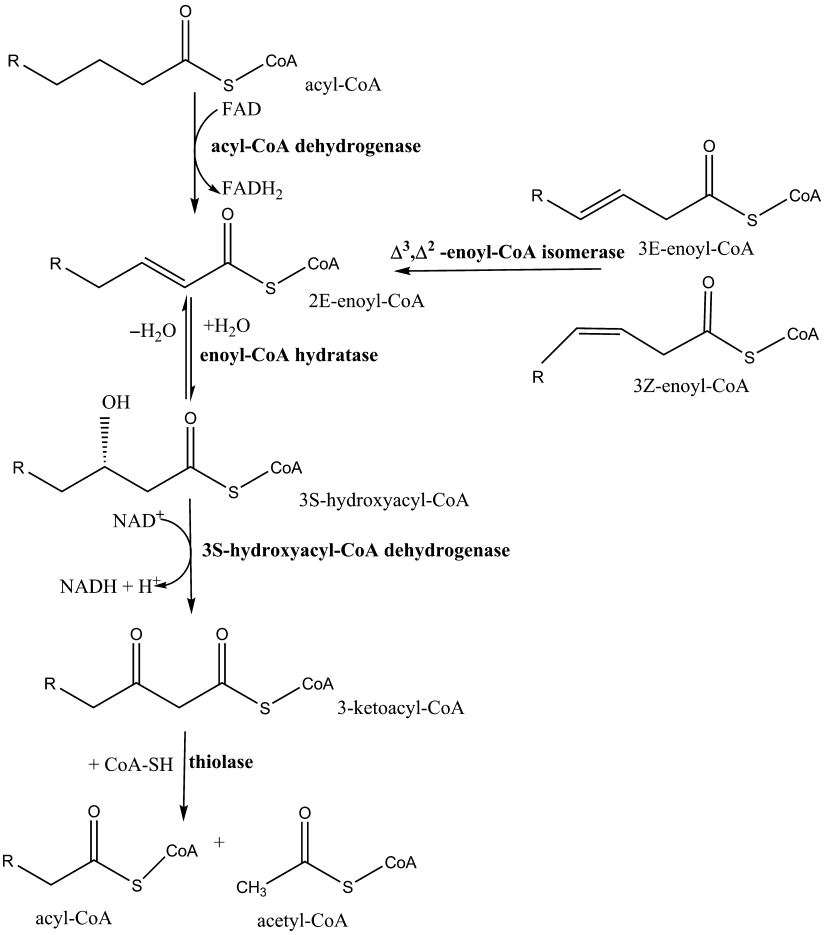

Fig. 1. The four reactions of the β-oxidation pathway. The Δ^3,Δ^2-enoyl-CoA isomerase reaction is the last reaction of the auxiliary pathway for the synthesis of 2E-enoyl-CoA from unsaturated fatty acyl-CoA having double bonds at odd positions or having Z double bonds.

(2X58) [10] and ECI from yeast peroxisomes (1PJH) [11]. Here, we report on structural enzymological studies of human ECI2 (HsECI2).

Each of the ECIs belongs to the crotonase fold superfamily of enzymes [12,13]. Crotonase is the original name of enoyl-CoA hydratase, type 1 (ECH), the structure of which was one of the first determined from this superfamily [14], together with the structure of a dehalogenase [15]. The crotonase fold is formed by approximately 300 residues. The superfamily includes many enzymes catalyzing a wide range of rather different reactions, using CoA thioesters as the substrate. Usually, these enzymes are trimers or hexamers (dimers of trimers). MFE1 is a monomer with two domains, and the enoyl-CoA isomerase active site is in the N-terminal crotonase domain. In this fold, there are two (mostly) parallel β-sheets (A and B). The edge strands A5 and B5 run anti-parallel to the other strands of these sheets (Fig. 2). The central β-sheet (sheet A) provides a structural framework. The strands of this sheet, termed A1–A4, continue into the β-strands of sheet B, termed B1–B4, and are then followed by helices H1–H4 forming the ββα-spiral crotonase fold. The β-strands of sheet B are rather short (Fig. 2).

For MFE1 [16], ECI1 [9] and ECH [17] (3ZWC, 1SG4 and 2DUB, respectively) the mode of binding of fatty acyl-CoA is known, adopting a bent conformation (Fig. 2). The CoA moiety binds between helix-10 and β-strands 1–3 of the β-sheet B. The loops emerging from the β-strands of β-sheet B and leading into the covering α-helices, in particular loop-1, loop-2, loop-3 and loop-4, play important roles in the CoA binding as well as in the catalytic process of these enzymes. Loop-2 is a long loop with variable length (Fig. 3A). Loop-3 is very short as strand B3 continues immediately into helix-3, which is the catalytic helix. A common feature in the active sites of each of these enzymes is an oxyanion hole (OAH), formed by two peptide NH groups of two different loops, loop-2 and loop-3/helix-3. Loop-2 is solvent exposed and is not involved in intratrimer subunit–subunit interactions, whereas the loop-3 region, being the N terminus of helix-3, is rather buried. In MFE1 and in ECH, loop-2 is involved in binding the fatty acyl tail, whereas in ECI1 the fatty acyl tail points towards loop-4 (between loop-4 and helix-9). In ECI1, the C-terminal end of loop-4, also referred to as the flap region (Fig. 3A), has adopted another conformation compared to MFE1 and ECH (and also in yeast ECI) (Fig. 2). ECI1 and ECI2 therefore form two distinct subfamilies within the crotonase superfamily, as is also found from phylogenetic relationships (Fig. 3B), showing also that the yeast ECI belongs to the ECI2 subfamily. The

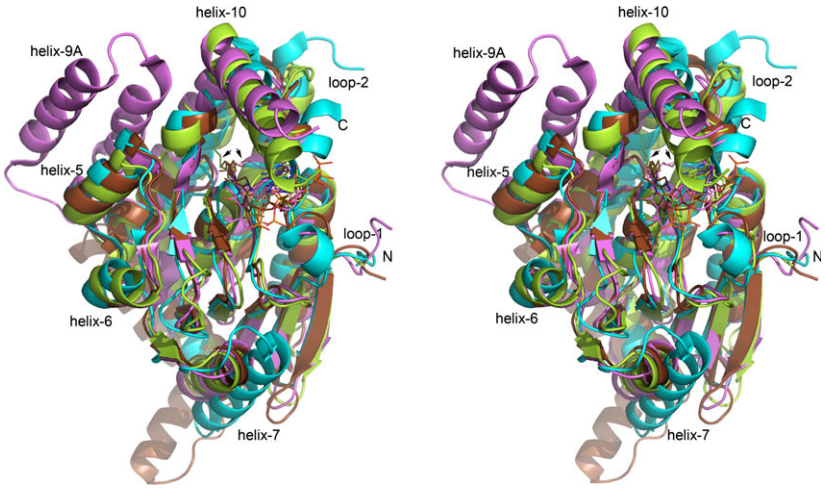

Fig. 2. The crotonase fold. Structural comparison of the superimposed structures of the crotonase domain of rat ECH (2DUB, brown, with bound octanoyl-CoA), MFE1 (3ZWC, N-terminal domain, lilac, with bound 3S-hydroxydecanoyl-CoA), human ECI1 (1SG4, lemon, with bound octanoyl-CoA) and yeast ECI2 (1PJH, cyan, unliganded). The labeled helix-5 is at the subunit–subunit interface of the trimers of the crotonase superfamily. The β-strand between helix-5 and helix-6 is the edge strand of sheet B, whereas some residues of loop-1 and loop-2 are forming the other edge of sheet B. Helix-7 shields β-sheet A from bulk solvent. The acyl-CoA is wedged between helix-10 and sheet B. The two black arrows show the two different binding modes of the fatty acyl tail. The 'left' mode of binding is found in ECI1, whereas the 'right' mode of binding is seen in ECH and MFE1. The structures of ECI1 and ECI2 represent the canonical crotonase fold, assembled in a trimer. MFE1 is a monomer and the additional helices, before helix-9 (helix-9A and the next helix), prevent trimerization. In ECH helices 9 and 10 have been swapped over to the neighboring subunit (not shown in this panel).

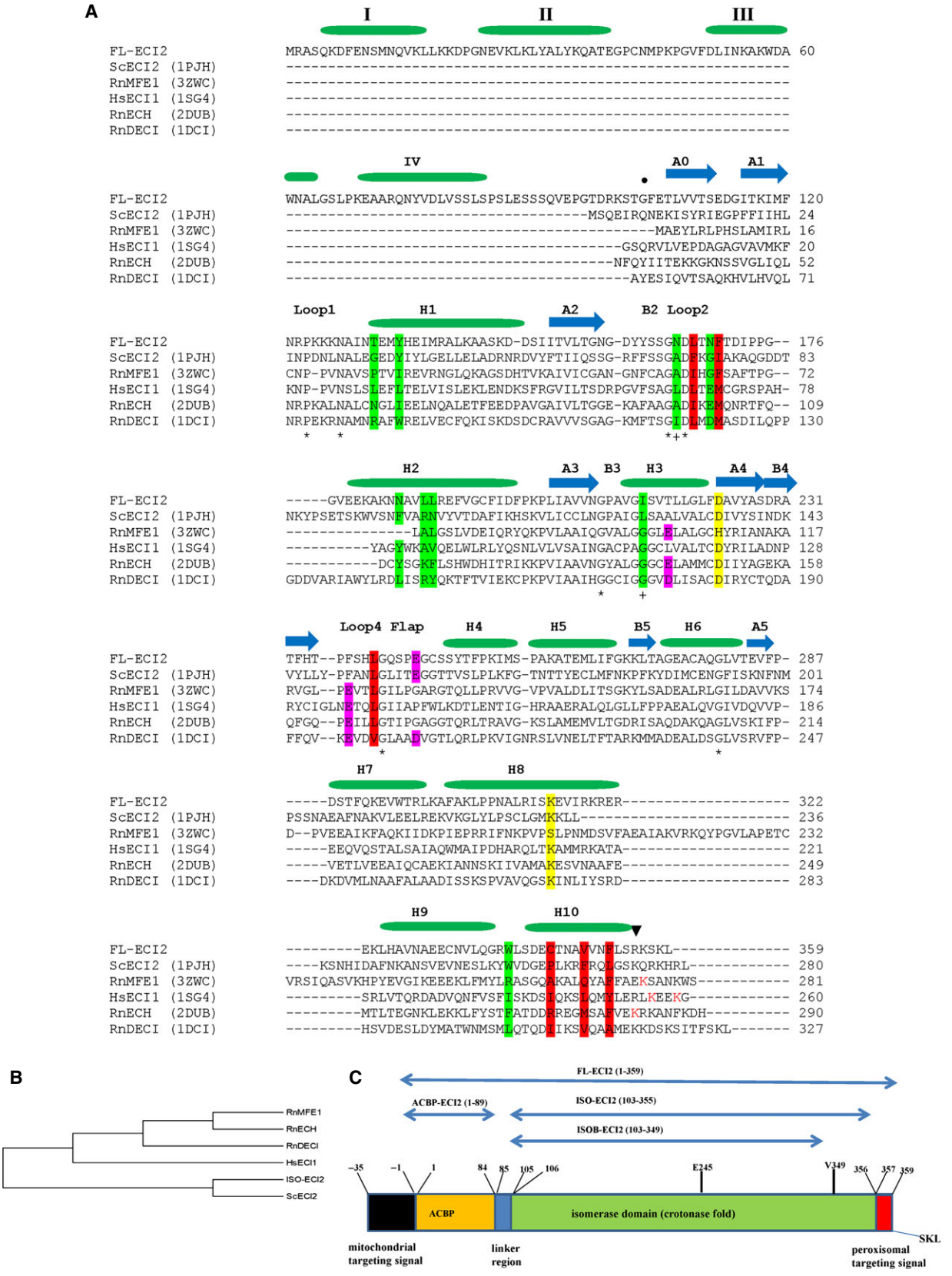
A
I
II
III
FL-ECI2 MRASQKDFENSMNQVKLLKKDPGNEVKLKLYALYKQATEGPCNMPKPGVFDLINKAKWDA 60
ScECI2 (1PJH)
RnMFE1 (3ZWC)
HsECI1 (1SG4)
RnECH (2DUB)
RnDECI (1DCI)
IV
A0
A1
FL-ECI2 WNALGSLPKEAARQNYVDLVSSLSPSLESSSQVEPGTDRKSTGFETLVVTSEDGITKIMF 120
ScECI2 (1PJH) MSQEIRQNEKISYRIEGPFFIIHL 24
RnMFE1 (3ZWC) MAEYLRLPHSLAMIRL 16
HsECI1 (1SG4) GSQRVLVEPDAGAGVAVMKF 20
RnECH (2DUB) NFQYIITEKKGKNSSVGLIQL 52
RnDECI (1DCI) AYESIQVTSAQKHVLHVQL 71
Loop1
H1
A2
B2
Loop2
FL-ECI2 NRPKKKNAINIEMYHEIMRALKAASKD-DSIITVLTGNG-DYYSSGNDLTNFTDIPPG-- 176
ScECI2 (1PJH) INPDNLNALEGEDYIYLGELLELADRNRDVYFTIIQSSG-RFFSSGADFKGIAKAQGDDT 83
RnMFE1 (3ZWC) CNP-PVNAVSPTVIREVRNGLQKAGSDHTVKAIVICGAN-GNFCAGADIHGFSAFTPG-- 72
HsECI1 (1SG4) KNP-PVNSLSLEFLTELVISLEKLENDKSFRGVILTSDRPGVFSAGLDLTEMCGRSPAH- 78
RnECH (2DUB) NRPKALNALCNGLIEELNQALETFEEDPAVGAIVLTGGE-KAFAAGADIKEMQNRTFQ-- 109
RnDECI (1DCI) NRPEKRNAMNPAFWRELVECFQKISKDSDCRAVVVSGAG-KMFTSGIDLMDMASDILQPP 130
H2
A3
B3
H3
A4
B4
FL-ECI2 -----GVEEKAKNNAVLLREFVGCFIDFPKPLIAVVNGPAVGISVTLLGLFDAVYASDRA 231
ScECI2 (1PJH) NKYPSETSKWVSNFVARNVYVTDAFIKHSKVLICCLNGPAIGLSAALVALCDIVYSINDK 143
RnMFE1 (3ZWC) LALGSLVDEIQRYQKPVLAAIQGVALGGGLELALGCHYRIANAKA 117
HsECI1 (1SG4) YAGYWKAVQELWLRLYQSNLVLVSAINGACPAGGCLVALTCDYRILADNP 128
RnECH (2DUB) DCYSGKFLSHWDHITRIKKPVIAAVNGYALGGGCELAMMCDIIYAGEKA 158
RnDECI (1DCI) GDDVARIAWYLRDLISRYQKTFTVIEKCPKPVIAAIHGGCIGGGVDLISACDIRYCTQDA 190
Loop4
Flap
H4
H5
B5
H6
A5
FL-ECI2 TFHT--PFSHLGQSPEGCSSYTFPKIMS-PAKATEMLIFGKKLTAGEACAQGLVTEVFP- 287
ScECI2 (1PJH) VYLLY-PFANLGLITEGGTTVSLPLKFG-TNTTYECLMFNKPFKYDIMCENGFISKNFNM 201
RnMFE1 (3ZWC) RVGL--PEVTLGILPGARGTQLLPRVVG-VPVALDLITSGKYLSADEALRLGILDAVVKS 174
HsECI1 (1SG4) RYCIGLNETQLGIIAPFWLKDTLENTIG-HRAAERALQLGLLFPPAEALQVGIVDQVVP- 186
RnECH (2DUB) QFGQ--PEILLGTIPGAGGTQRLTRAVG-KSLAMEMVLTGDRISAQDAKQAGLVSKIFP- 214
RnDECI (1DCI) FFQV--KEVDWGLAADVGTLQRLPKVIGNRSLVNELTFTARKMMADEALDSGLVSRVFP- 247
H7
H8
FL-ECI2 -----DSTFQKEVWTRLKAFAKLPPNALRISKEVIRKRER---------- 322
ScECI2 (1PJH) PSSNAEAFNAKVLEELREKVKGLYLPSCLGMKKLL---------- 236
RnMFE1 (3ZWC) D--PVEEAIKFAQKIIDKPIEPRRIFNKPVPSLPNMDSVFAEAIAKVRKQYPGVLAPETC 232
HsECI1 (1SG4) -----EEQVQSTALSAIAQWMAIPDHARQLTKAMMRKATA---------- 221
RnECH (2DUB) -----VETLVEEAIQCAEKIANNSKIIVAMAKESVNAAFE---------- 249
RnDECI (1DCI) ----DKDVMLNAAFALAADISSKSPVAVQGSKINLIYSRD---------- 283
H9
H10
FL-ECI2 ---------EKLHAVNAEECNVLQGRWLSDECTNAVVNFLSRKSKL---------- 359
ScECI2 (1PJH) ----KSNHIDAFNKANSVEVNESLKYWVDGEPLKRFRQLGSKQRKHRL---------- 280
RnMFE1 (3ZWC) VRSIQASVKHPYEVGIKEEEKLFMYLRASGQAKALQYAFFAEKSANKWS---------- 281
HsECI1 (1SG4) ---------SRLVTQRDADVQNFVSFISKDSIQKSLQMLERLKEEKG---------- 260
RnECH (2DUB) ---------MTLTEGNKLEKKLFYSTFATDDRREGMSAFVEKRKANFKDH---------- 290
RnDECI (1DCI) ---------HSVDESLDYMATWNMSMLQTQDIIKSVQAAMEKKDSKSITFSKL------- 327
B
RnMFE1
RnECH
RnDECI
HsECI1
ISO-ECI2
ScECI2
C
FL-ECI2 (1-359)
ACBP-ECI2 (1-89)
ISO-ECI2 (103-355)
ISOB-ECI2 (103-349)
−35
−1
1
84
85
105
106
E245
V349
356
357
359
ACBP
isomerase domain (crotonase fold)
SKL
mitochondrial targeting signal
linker region
peroxisomal targeting signal

sequences of the enzymes of the crotonase superfamily are rather diverse [12,13], as is also evident from the sequence alignment of the sequences of human ECI2 with the hexameric yeast ECI2 (22% sequence identity), the monomeric rat MFE1 (19% sequence identity), the trimeric human ECI1 (17% sequence identity), the hexameric rat ECH (23% sequence identity) and the hexameric rat DECI (21% sequence identity).

In ECIs [8,9,18] the catalytic residue is a glutamate, which abstracts a proton from the substrate C2 atom, generating a negatively charged enolate [19]. The negative charge of the thioester oxygen atom is stabilized by the OAH [20,21]. Subsequently, the abstracted proton is transferred to the C4 atom, generating the 2E-enoyl-CoA product (Fig. 1). From sequence (Fig. 3) and structural alignments (Fig. 2), it can be inferred that this glutamate in HsECI2 is Glu245, protruding out of the flap region (end of loop-4, just before helix-4) into the catalytic site, whereas the OAH is formed by the peptide NH moieties of Asn165 (loop-2) and Ile214 (helix-3).

A peculiar property of mammalian ECI2 is the presence of the 80 residue long acyl-CoA binding (ACBP) domain at its N terminus (Fig. 3A), which is connected to the isomerase domain by a linker region. This extra domain is not present in yeast ECI2. The NMR structure of the ACBP domain of HsECI2 is known (2CQU; Tsubota *et al.*; unpublished), having the same four helical bundle fold as human liver ACBP (2CB8) [22]. The four helices of the ACBP of HsECI2 are labeled in Fig. 3A. This extra domain is not present in yeast ECI2 and its function in mammalian ECI2 is not clear. Such an extra lipid-molecule binding domain of unknown function is also found in some other peroxisomal enzymes, such as in the mammalian sterol carrier protein type 2 (SCP2) thiolase (having an extra SCP2 domain) [23] and in peroxisomal multifunctional enzyme type 2 (MFE2) (also having an SCP2 domain) [24,25]. A common structural feature of every crotonase enzyme is helix-10. This is the C-terminal helix, which is anchored at its N terminus to the rest of the protein at the subunit–subunit interface. Its C terminus covers the active site and the CoA binding pocket and points into bulk solvent, being disordered in many structures. A conserved feature of helix-10 is the presence of one or two basic residues, which interact with the phosphate moieties of the substrate in enzyme–substrate complexes [9,16,17].

It has been noted that the crotonase fold is frequently used in nature to generate natural enzymes covering a wide range of substrate and reaction specificities, always using the OAH for its biocatalytic properties [13,19]. This has recently been exploited for the creation of non-natural enzymes [26–28] catalyzing the formation of C–C bonds. The current study was also undertaken to provide better understanding of the functional importance of various modules, like helix-10 and the ACBP domain, taking HsECI2 as the reference molecule. Structural enzymological properties of HsECI2 were investigated by performing solution small angle X-ray scattering (SAXS), X-ray crystallography, calorimetry and enzyme kinetics studies. The properties of the full-length construct (FL-ECI2) have been compared with the properties of a truncated variant lacking the ACBP domain (ISO-ECI2) as well as with the ACBP domain itself (ACBP-ECI2). In addition the properties of the truncated enzyme derived from ISO-ECI2 in which helix-10 has

Fig. 3. (A) The structure based sequence alignment of isomerases and hydratases of the crotonase superfamily. The secondary structure above the sequence refers to the human ISO-ECI2 structure as assigned by DSSP. The secondary structure of the ACBP domain concerns its NMR structure (2CQU). The sequence numbering refers to the Uniprot sequence concerning HsECI2 (O75521) and to the PDB entries of *S. cerevisae* peroxisomal ECI2 (ScECI2, 1PJH), the crotonase domain of rat peroxisomal MFE1 (RnMFE1, 3ZWC), human mitochondrial ECI1 (HsECI1, 1SG4), rat mitochondrial ECH (RnECH, 2DUB) and rat DECI (RnDECI, 1DCI). The fully conserved residues are labeled by an asterisk. The residues forming the OAH are marked by a plus sign. The black dot (●), at Gly103, marks the first residue of the ISO-ECI2, ISOA-ECI2 and ISOB-ECI2 variants, preceded by the purification tag. The C-terminal end of ISO-ECI2 and ISOA-ECI2 is marked with an arrow (▼). The catalytic residues are highlighted in purple. The residues highlighted in red form the hydrophobic cluster near the thioester and adenine moiety of the substrate, as known from structures of complexes, fixing helix-10 with respect to loop-2 and loop-4. The residues highlighted in green form the tunnel of the fatty acyl binding pocket. The basic residues of helix-10 known to interact in complexes with the phosphate moieties of the ligand are colored in red. (B) The evolutionary relationships of the six sequences aligned in (A). The percentages of replicate trees in which the associated taxa clustered together in the bootstrap test (10 000 replicates) are shown next to the branches. The tree is drawn to scale, with branch lengths in the same units as those of the evolutionary distances used to infer the phylogenetic tree. (C) The modular structure of ECI2. The constructs used in these studies are visualized. Each of these constructs includes a purification tag just before Gly103 for the ISO-ECI2, ISOA-ECI2 and ISOB-ECI2 constructs, and just before Met1 for FL-ECI2 and ACBP-ECI2. E245 is the catalytic glutamate. V349 is the mutated residue (V349A) of ISOA-ECI2.

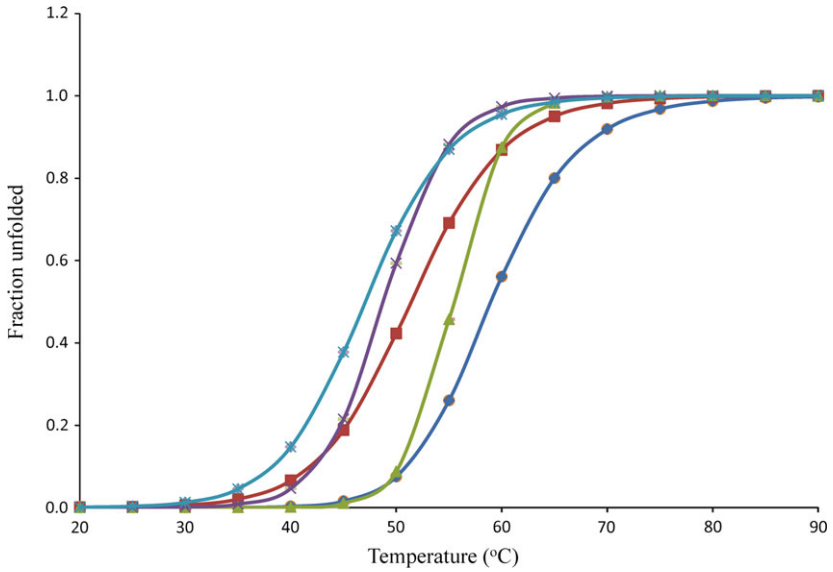

Fig. 4. The CD melting curves showing the calculated percentages of unfolded protein as a function of temperature. The calculated T_m values are 57.0 ± 1.4 °C for FL-ECI2 (cyan), 55.4 ± 0.1 °C for ISO-ECI2 (green), 51.4 ± 0.1 °C for ACBP-ECI2 (red), 48.9 ± 0.2 °C for ISOA-ECI2 (purple) and 47.0 ± 0.3 °C for ISOB-ECI2 (light blue).

been mutated, either by a point mutation V349A (ISOA-ECI2) or by deleting the C-terminal residues 350–355 (ISOB-ECI2), were studied. The precise constructs that have been used are visualized in Fig. 3C. Crystal structures of the truncated enzyme and its two helix-10 variants show the active site geometry of HsECI2 as well as the structural effects of mutations in helix-10.

Results and discussion

The purified FL-ECI2 and ISO-ECI2 behave as trimers in solution as shown by static light scattering (SLS), having molecular masses of 133.5 and 89 kDa, respectively. Using circular dichroism (CD) spectroscopy it was found that these constructs, as well as the ACBP-ECI2 variant, are properly folded proteins. Stability studies have been done with FL-ECI2, ISO-ECI2 and ACBP-ECI2 by measuring the CD melting curves as a function of temperature (Fig. 4). These data show that ISO-ECI2 is a stable protein (melting temperature T_m = 55.4 °C), being somewhat less stable than FL-ECI2 (T_m = 57.0 °C), whereas the T_m of ACBP-ECI2 is 51.4 °C. Enzyme kinetics measurements show that ISO-ECI2 can isomerize 3E-hexenoyl-CoA and 3E-decenoyl-CoA to the corresponding 2E-acyl-CoA molecules (Table 1). The Michaelis–Menten enzyme kinetics parameters show that the ISO-ECI2 construct is less active than the wild-type FL-ECI2 enzyme. For example the k_{cat} for the 3E-decenoyl-CoA substrate is 56 s^{-1} for FL-ECI2 and 7.5 s^{-1} for ISO-ECI2, whereas the K_m value changes somewhat, from 83 to 31 μM. The variation of the kinetic properties of FL-ECI2 from short-chain to long-chain substrates shows the same trend as observed for the rat ECI2 [6]: the k_{cat} values increase and the K_m values decrease for longer chain substrates. The differences of the FL-ECI2 and ISO-ECI2 Michaelis–Menten parameters indicate that the presence of the ACBP domain influences the enzyme kinetics properties. Indeed, calorimetric affinity data using the saturated decanoyl-CoA (substrate analogue) and 3E-decenoyl-CoA (substrate) as ligand with the ACBP-ECI2 construct indicate that the ACBP domain has high affinity for both of these ligands, with a K_d of 1.5 μM for the saturated decanoyl-CoA (substrate analogue) (Table 2) and 5 μM for

Table 1. The Michaelis–Menten parameters of FL-ECI2 and ISO-ECI2. The standard deviations are based on three independent experiments.

Enzyme: substrate	K_m (μM)	k_{cat} (s^{-1})	k_{cat}/K_m ($s^{-1}\cdot M^{-1}$)
FL-ECI2			
3E-hexenoyl-CoA	138.5 ± 48.7	20.2 ± 3.6	1.5 × 10^5
3E-decenoyl-CoA	83.4 ± 24.6	56.3 ± 9.3	6.7 × 10^5
ISO-ECI2			
3E-hexenoyl-CoA	446.0 ± 11.2	11.6 ± 5.0	0.3 × 10^5
3E-decenoyl-CoA	31.0 ± 4.3	7.5 ± 0.3	2.4 × 10^5

Table 2. The calorimetric data as obtained from the ITC experiments. The error estimates, difference from the mean, are based on two independent experiments. NB indicates no binding detected.

Enzyme	Substrate analogues	$K_a \times 10^5$ (M^{-1})	K_d (μM)	$-T\Delta S$ (kcal·mol^{-1})	ΔH (kcal·mol^{-1})	N (number of sites)	ΔG (kcal·mol^{-1})
FL-ECI2	Octanoyl-CoA	1.92 ± 0.84	5.21	−4.60 ± 0.10	−2.54 ± 0.38	2.19 ± 0.00	−7.14
	Decanoyl-CoA	7.10 ± 1.90	1.42	−3.61 ± 1.10	−4.36 ± 0.86	2.03 ± 0.01	−7.97
	Lauroyl-CoA	27.45 ± 2.01	0.36	−4.32 ± 0.20	−4.53 ± 0.17	2.02 ± 0.03	−8.85
	Myristoyl-CoA	2.13 ± 0.95	4.69	−4.23 ± 0.40	−2.96 ± 0.09	3.87 ± 0.09	−7.19
ISO-ECI2	Octanoyl-CoA	0.032 ± 0.01	313.00	1.11 ± 0.22	−5.62 ± 0.62	1.05 ± 0.05	−4.51
	Decanoyl-CoA	0.27 ± 0.16	37.04	−1.17 ± 0.66	−4.74 ± 0.91	1.33 ± 0.09	−5.91
	Lauroyl-CoA	0.82 ± 0.23	12.20	−1.36 ± 0.24	−5.32 ± 0.40	1.35 ± 0.29	−6.68
	Myristoyl-CoA	0.65 ± 0.25	15.39	−2.40 ± 0.43	−4.12 ± 0.67	1.69 ± 0.59	−6.52
ACBP-ECI2	Octanoyl-CoA	1.90 ± 0.86	5.26	−4.63 ± 0.38	−2.51 ± 0.66	1.14 ± 0.03	−7.14
	Decanoyl-CoA	6.57 ± 0.11	1.52	−4.78 ± 0.49	−3.15 ± 0.48	0.84 ± 0.16	−7.93
	Lauroyl-CoA	38.35 ± 11.25	0.26	−4.34 ± 0.97	−4.62 ± 1.15	1.30 ± 0.28	−8.96
	Myristoyl-CoA	38.55 ± 0.35	0.26	−4.96 ± 0.05	−4.02 ± 0.05	1.52 ± 0.04	−8.98
ISOA-ECI2	Octanoyl-CoA	NB	NB	NB	NB	NB	NB
	Decanoyl-CoA	0.40 ± 0.07	25.00	1.83 ± 0.03	−8.06 ± 0.08	1.23 ± 0.00	−6.23
	Lauroyl-CoA	0.94 ± 0.04	10.60	3.34 ± 0.09	−10.11 ± 0.14	1.14 ± 0.04	−6.77
ISOB-ECI2	Octanoyl-CoA	NB	NB	NB	NB	NB	NB
	Decanoyl-CoA	0.99 ± 0.01	10.10	7.7 ± 0.39	−14.51 ± 0.38	0.66 ± 0.10	−6.81
	Lauroyl-CoA	1.81 ± 0.05	5.50	4.83 ± 0.18	−11.96 ± 0.21	1.10 ± 0.01	−7.13

the substrate 3E-decenoyl-CoA. These dissociation constants are at least 10-fold lower than the K_m values measured for the 3E-decenoyl-CoA substrate with FL-ECI2 (K_m = 83.4 μM) and ISO-ECI2 (K_m = 31.0 μM). The calorimetric data also show that there is one binding site per ACBP molecule. Calorimetric experiments with a range of substrate analogues with FL-ECI2 show that there are two binding sites per subunit, in agreement with the binding of these ligands to both the ACBP-ECI2 domain and the ISO-ECI2 domain. The ACBP-ECI2 domain has much higher affinity than the ISO-ECI2 domain for each of the tested saturated acyl-CoA substrate analogues (Table 2). This is true for ligands with fatty acyl tails of different lengths, varying from octanoyl-CoA to myristoyl-CoA, and it is most pronounced for ligands having the short tail lengths of octanoyl-CoA and decanoyl-CoA. For example the K_d values of ACBP-ECI2 and ISO-ECI2 for the saturated decanoyl-CoA substrate analogue are 1.5 and 37 μM, respectively.

The acyl-CoA binding sites of the ACBP and isomerase domains are rather different. Crystallographic [22,29] and NMR [30] binding studies with ACBP have revealed that the ACBP binding site is a groove, binding acyl-CoA in such a way that the adenine moiety is stacked between a tyrosine and the fatty acyl tail, which subsequently interacts with hydrophobic side chains. In the spiral-like conformation the pantetheine part is bulk solvent exposed, being modeled in the NMR structure [30] but disordered in the crystal structure of the plasmodium ACBP complex [29]. To the crotonase fold, acyl-CoA is bound in the characteristic bent conformation (Fig. 2). The differences in the mode of binding of acyl-CoA to ACBP and the crotonase domain indeed result in different thermodynamic profiles of acyl-CoA binding to the ACBP-ECI2 domain and the ISO-ECI2 domain. The binding of acyl-CoA to the ISO-ECI2 domain is mainly enthalpy driven, whereas the binding to the ACBP-ECI2 domain is mainly entropy driven (Table 2).

Structure of full-length HsECI2 in solution

To gain an insight into the assembly of the full-length HsECI2 enzyme, structural studies were carried out in solution using X-ray scattering. Different modeling approaches were taken, ranging from *ab initio* bead- and chain-like models to hybrid modeling utilizing known structures of the isomerase trimer and the ACBP domain. In essence, all modeling approaches gave the same overall results, with very good fits to the raw X-ray scattering data.

The SAXS experiments show that both FL-ECI2 and ISO-ECI2 are trimers in solution (Table 3, Fig. 5). The theoretical scattering curve from the ISO-ECI2 crystal structure fits the corresponding SAXS data well, validating the trimeric conformation observed in the crystal structure. On the other hand, as expected, the ACBP domain is a monomer (Table 3, Fig. 5); the slight misfit between the SAXS data and the crystal structure (Fig. 5A) relates to the fact that our ACBP construct is significantly longer, having an extra 27 res-

Table 3. SAXS analysis of the HsECI2 constructs. $I(0)$ and R_g were determined for FL-ECI2 from 4 to 12 samples in the absence and presence of ligand, respectively. The molecular mass (MM) was calculated from the estimated Porod volume based on the partial specific volume of 0.7425 $cm^3 \cdot g^{-1}$ [55]. The chi values for fitting the crystal structures to the raw SAXS data are from CRYSOL.

Sample	Monomer MM from sequence (kDa)	MM based on $I(0)$ (kDa)	R_g (Å)	D_{max} (Å)	MM based on Porod volume (kDa), ratio to MM from sequence	Fit of structural model to SAXS data (chi)
FL-ECI2 (no ligand)	41.3	93 ± 9	44.8 ± 1.2	160	130, 3.1	0.89 (BUNCH), 0.84 (CORAL), 1.5 (GASBOR), 0.97 (DAMMIF)
FL-ECI2 (ligand)	41.3	106 ± 12	44.5 ± 2.1	–	–	–
ISO-ECI2	31.0	93	32.3	120	100, 3.2	1.3 (GASBOR)
ACBP-ECI2	11.6	17	19.2	80	12, 1.0	1.0 (GASBOR)
ISO-ECI2 crystal structure (this study)	–	–	27	90	–	1.3
ACBP crystal structure (2FJ9)	–	–	13.6	46.2	–	1.8

idue long purification tag, which is predicted to be disordered. The positions of the ACBP domains in the full-length enzyme are such that the ACBP domains do not physically interact with each other. The ACBP domains extend away from the ISO-ECI2 core and lie in the same plane as the flattened isomerase domain trimer, at the corners of a triangle (Fig. 5C & E). Thus, the full-length enzyme is a highly flattened trimer in solution. Apparently, the ACBP domain adopts a well defined position with respect to the core trimer; whether it has additional flexibility or motility cannot be assessed with the current data. In the FL-ECI2 model, the binding pockets of the ACBP and ISO-ECI2 domains of the same polypeptide chain are facing each other, being separated by 40 Å, as measured between the N3 atoms of the adenine moieties of the superimposed models (Fig. 5G). The SAXS data for the apo and complexed forms of FL-ECI2 show that the shape of FL-ECI2 with and without ligand is the same, as the scattering curves have identical shapes (Table 3, Fig. 5F). Thus, there are no large-scale conformational changes in HsECI2 related to acyl-CoA ligand binding.

The enzymological comparison of FL-ECI2 and ISO-ECI2 suggests an *in vivo* function for the ACBP domain; the ACBP domain of FL-ECI2 makes the enzyme more proficient compared to ISO-ECI2, especially for short-chain fatty acyl-CoA substrates. For example, for the 3E-hexenoyl-CoA substrate, the k_{cat}/K_m value changes from 1.5×10^5 $M^{-1} \cdot s^{-1}$ for FL-ECI2 to 0.3×10^5 $M^{-1} \cdot s^{-1}$ for ISO-ECI2 (Table 1). It is not clear from the FL-ECI2 SAXS model how the presence of the ACBP domain enhances catalytic proficiency, as conformational changes induced by ligand binding were not detected. The large distance (Fig. 5G) between the binding pockets of the ACBP and isomerase domains in the same subunit indicates that the fatty acyl moiety cannot reach its binding site in the isomerase domain, while the adenine part is still bound to ACBP. It is possible that the ACBP domain initially captures the substrate and subsequently delivers it via a transient movement towards the active

Fig. 5. SAXS analysis of HsECI2. (A) SAXS scattering data for ISO-ECI2 (left), FL-ECI2 (middle) and ACBP-ECI2 (right). The shown fits (from left to right) represent the ISO-ECI2 crystal structure from this study, the BUNCH hybrid model of FL-ECI2 (see E) and the crystal structure of human ACBP (2FJ9). The inset in the right graph shows a superposition of a GASBOR *ab initio* chain-like model of ACBP-ECI2 (gray) and the ACBP crystal structure (2FJ9; green). The Guinier plots below each scattering curve indicate good linear fitting for all samples. (B) The *ab initio* GASBOR model of ISO-ECI2 (gray) superimposed with the crystal structure of ISO-ECI2. (C) The GASBOR model of FL-ECI2 (gray) with the superimposed crystal structure of the ISO-ECI2 trimer in the middle surrounded by three ACBP molecules (1ACA). The latter model is based on the BUNCH model of (E) but the ACBP-ECI2 part was replaced by the coordinates of the NMR structure of bovine ACBP (1ACA) complexed with palmitoyl-CoA (shown in orange). (D) Distance distribution functions for FL-ECI2 (black), ISO-ECI2 (red) and ACBP-ECI2 (blue). (E) Hybrid model of FL-ECI2 made using BUNCH. ACBP and isomerase domains are green and cyan, respectively. The linker regions (Pro85-Glu105) and N and C termini are shown in magenta. (F) SAXS data for unliganded (topmost curve) and three liganded samples of FL-ECI2 (top to bottom: octanoyl-CoA, decanoyl-CoA, lauroyl-CoA). (G) Zoomed-in view of the FL-ECI2 model showing the acyl-CoA binding sites of the isomerase and ACBP domains. The model is the same as shown in (C) except that the dummy atom BUNCH model of the linker region is also shown. The acyl-CoA product, 3S-hydroxydecanoyl-CoA, modeled in the isomerase domain is from the superimposed structure of MFE1 hydratase (3ZWC). The red arrow marks the N terminus of the catalytic helix, helix-3.

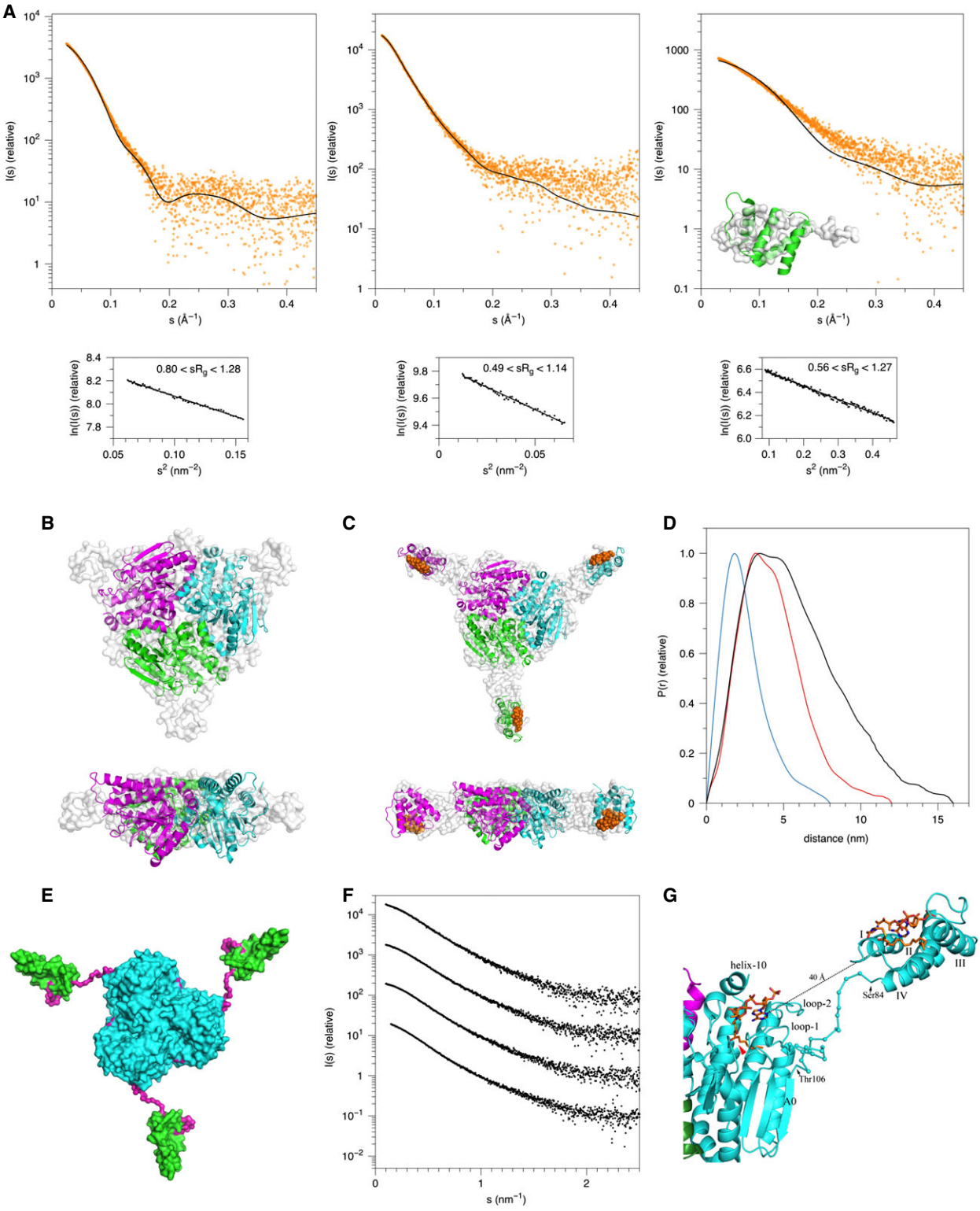
A
I(s) (relative)
s (Å^{-1})
ln(I(s)) (relative)
s^2 (nm^{-2})
0.80 < sR$_g$ < 1.28
0.49 < sR$_g$ < 1.14
0.56 < sR$_g$ < 1.27
B
C
D
P(r) (relative)
distance (nm)
E
F
I(s) (relative)
s (nm^{-1})
G
helix-10
40 Å
Ser84
loop-2
loop-1
Thr106
A0
I
II
III
IV

site of ISO-ECI2. Alternatively, this transfer of substrate can happen by diffusion over the surface from the ACBP binding site to the isomerase binding site, or by a combination of these two possibilities. Diffusion through bulk solvent would require an additional solvation and desolvation step. In any case, the rate-limiting step in the complete isomerase reaction cycle is unknown, and the function of the ACBP domain could also be related to product release.

The ISO-ECI2 crystal structure

The ISO-ECI2 crystals were grown at pH 6.5 in the presence of 1 M ammonium sulfate (Table 4). The crystal structure of ISO-ECI2, refined at 2.6 Å resolution (Table 5), reveals its trimeric structure (Fig. 6A). Although the crystals were grown in the presence of 0.5 mM decanoyl-CoA, the ligand is not present in any of the three active sites. Numerous additional co-crystallization and crystal soaking experiments with various acyl-CoA ligands did not result in crystals of the corresponding ligand ISO-ECI2 complexes. The most flexible region is loop-2. It is best defined and completely built in subunit A, but poorly ordered in subunit B in which residues Phe170-Thr171-Asp172-Ile173 could not be built. In subunit C also a complete trace of loop-2 could be modeled adopting a similar conformation as in subunit A. The side chains of Phe170 and Leu167 of loop-2 point towards the side chain of Val349 of helix-10. In subunit A, a glycerol molecule is bound in the active site, being hydrogen bonded to N(Asn165) and N(Ile214), which are the OAH forming NH groups, while a chloride ion is bound in each of the three subunits (Fig. 6A).

Extensive structural comparisons were done with the liganded structures of MFE1, ECH and ECI1. The active site loops, loop-1, the beginning of loop-2, loop-3 and the beginning of loop-4, adopt the same conformations as is known from yeast ECI2, MFE1 and ECH (Figs 6 and 7). The catalytic glutamate points from the flap region of loop-4 into the active site. The structures of MFE1, complexed with 3S-hydroxydecanoyl-CoA (3ZWC), and ECH, complexed with octanoyl-CoA (2DUB), define the importance of loop-1 and loop-2 for the mode of binding of the 3′-phosphate-adenosine part of the CoA moiety. The adenine moiety of acyl-CoA is bound in a bulk solvent exposed binding pocket, shaped by β-strand B1/loop-1 and β-strand B2/loop-2 (Fig. 6). The loop-1 residues involved in this binding pocket are Ala57-Leu58-Asn59-Ala60 in ECH and Pro20-Val21-Asn22-Ala23 in MFE1. The corresponding residues in ISO-ECI2 are Lys125-Lys126-Asn127-Ala128. The loop-2 residues of this binding pocket are Ala96-Gly97-Ala98-Asp99-Ile100 in ECH, Ala59-Gly60-Ala61-Asp62-Ile63 in MFE1 and Ser163-Gly164-Asn165-Asp166-Leu167 in ISO-ECI2 (Fig. 3). Each of these loops has highly conserved features such as an asparagine in loop-1 (Asn127 in HsECI2) and an aspartate in loop-2 (Asp166). The side chains of these conserved residues stabilize the local conformation by being hydrogen bonded to main chain atoms of the respective turns. These two conserved

Table 4. The buffers used for the purification and crystallization experiments. The size-exclusion buffer is also the protein storage buffer.

	Purification buffers			Crystallization buffers	
Variants	Lysis buffer	Affinity chromatography buffer	Size-exclusion buffer	Well solution buffer	Cryo buffer
ISO-ECI2	50 mM HEPES pH 7.5 300 mM NaCl	30 mM HEPES pH 7.5 150 mM NaCl 30 mM imidazole (wash)/ 500 mM imidazole (elution)	30 mM HEPES pH 7.5 100 mM NaCl	100 mM MES pH 6.5 1 M $(NH_4)_2SO_4$	100 mM MES pH 6.5 1 M $(NH_4)_2SO_4$ 0.2 mM decanoyl-CoA 20% glycerol
ISOA-ECI2	50 mM HEPES pH 7.5 300 mM NaCl	30 mM HEPES pH 7.5 150 mM NaCl 30 mM imidazole (wash)/ 500 mM imidazole (elution)	30 mM HEPES pH 7.5 100 mM NaCl	100 mM HEPES pH 7.5 10% PEG 6000 5% MPD	100 mM HEPES pH 7.5 10% PEG 6000 5% MPD 0.2 mM lauroyl-CoA 20% glycerol
ISOB-ECI2	50 mM Tris/HCl pH 7.5 300 mM NaCl 1 mM β-mercaptoethanol 10% glycerol	30 mM Tris/HCl pH 7.5 300 mM NaCl 1 mM β-mercaptoethanol 10% glycerol 30 mM imidazole (wash)/ 250 mM imidazole (elution)	30 mM HEPES pH 7.5 300 mM NaCl	80 mM sodium cacodylate pH 6.5 14.4% PEG 8000 160 mM calcium acetate	80 mM sodium cacodylate pH 6.5 14.4% PEG 8000 160 mM calcium acetate 20% glycerol

MPD: 2-Methyl-2, 4-pentanediol.

Table 5. The crystallographic statistics of data collection and structure refinement. The Ramachandran values are as calculated by MOLPROBITY [49].

	ISO-ECI2	ISOA-ECI2	ISOB-ECI2
Processing software	XDS	XDS	XDS
Scaling and merging	AIMLESS	AIMLESS	XDS
Beamline	ID29 (ESRF)	ID29 (ESRF)	I03 (DLS)
Wavelength (Å)	0.976	0.976	0.976
Spacegroup	$P2_12_12_1$	$P2_12_12_1$	$P2_12_12_1$
Unit cell parameters (Å)	76.43, 91.92, 130.37	47.61, 123.69, 128.93	74.44, 95.34, 129.97
Number of subunits per a.u	3	3	3
Resolution range (Å)[a]	49.6–2.64 (2.73–2.64)	47.61–1.88 (1.95–1.88)	34.85–2.85 (3–2.85)
Completeness (%)	98.4 (87.3)	99.5 (96.8)	99.6 (97.6)
$\langle I/\sigma \rangle$	11.5 (1.4)	12.0 (1.5)	9.9 (2.8)
R_{pim} (%)	4.4 (53.0)	5.4 (57.6)	6.7 (32.7)[b]
Number of unique reflections	27 223 (2323)	62 659 (5888)	22 266 (3146)
Multiplicity	7.9 (5.8)	7.2 (7.0)	5.7 (5.5)
Matthews coefficient (Å^3/Da)	2.5	2.1	2.6
Solvent content (%)	50.8	40.8	52.3
Wilson *B*-factor (Å^2)	82.1	31.5	49.8
Refinement statistics			
Resolution (Å)	49.6–2.64	47.6–1.88	34.9–2.85
R_{work} (%)	19.43	18.39	17.63
R_{free} (%)	26.22	23.44	23.30
Number of reflections (R_{work})	25 794	59 362	21 084
Number of reflections (R_{free})	1365	3172	1113
Number of atoms	5773	6072	5746
Number of waters	21	273	37
Number of ligand molecules			
Glycerol	1	–	–
Cl^-	3	3	3
Ethylene glycol	–	1	–
Geometry statistics			
rmsd, bonds (Å)	0.013	0.016	0.011
rmsd, angles (°)	1.5	1.7	1.4
Average *B*-factor (Å^2)			
Protein atoms	80.4	38.5	52.1
Waters	59.0	41.3	36.1
Glycerol	93.8	–	–
Cl^-	102.9	81.4	82.7
Ethylene glycol	–	48.0	–
Ramachandran plot (%)			
Favored	95.0	96.6	95.3
Allowed	99.0	99.6	99.2
Outliers	1.0	0.4	0.8
PDB ID	4U18	4U19	4U1A

[a] Values in parentheses are for the high resolution shells. [b] Calculated with AIMLESS [44].

turns are hydrogen bonded to each other via O(Gly60, loop-2) to N(Val24, loop-1) in MFE1 (3ZWC) and via O(Gly164, loop-2) to N(Ile129, loop-1) in HsECI2 (Fig. 6). In MFE1, the peptide NH group of the O (Gly60)–N(Ala61) peptide bond is one of the OAH hydrogen bond donors. The adenine is wedged between Ala60 and Ile100 in ECH and Ala23 and Ile63 in MFE1 (Fig. 6B). The corresponding residues in ISO-ECI2 are Ala128 and Leu167. The adenine-NH2 moiety is hydrogen bonded to O(Ala96) and O(Ala98) of loop-2 in ECH. These residues are Ala61 and Ala63 in MFE1 and Ser163 and Asn165 in HsECI2 (Fig. 6). The catalytic site, near the thioester moiety, is deeply buried at the N-terminal end of helix-3, as known from the mode of ligand binding to rat ECH [17] and MFE1 [16] (Fig. 2), having the fatty acyl tail buried in a tunnel lined by loop-2 residues and extending from the catalytic site to the bulk solvent.

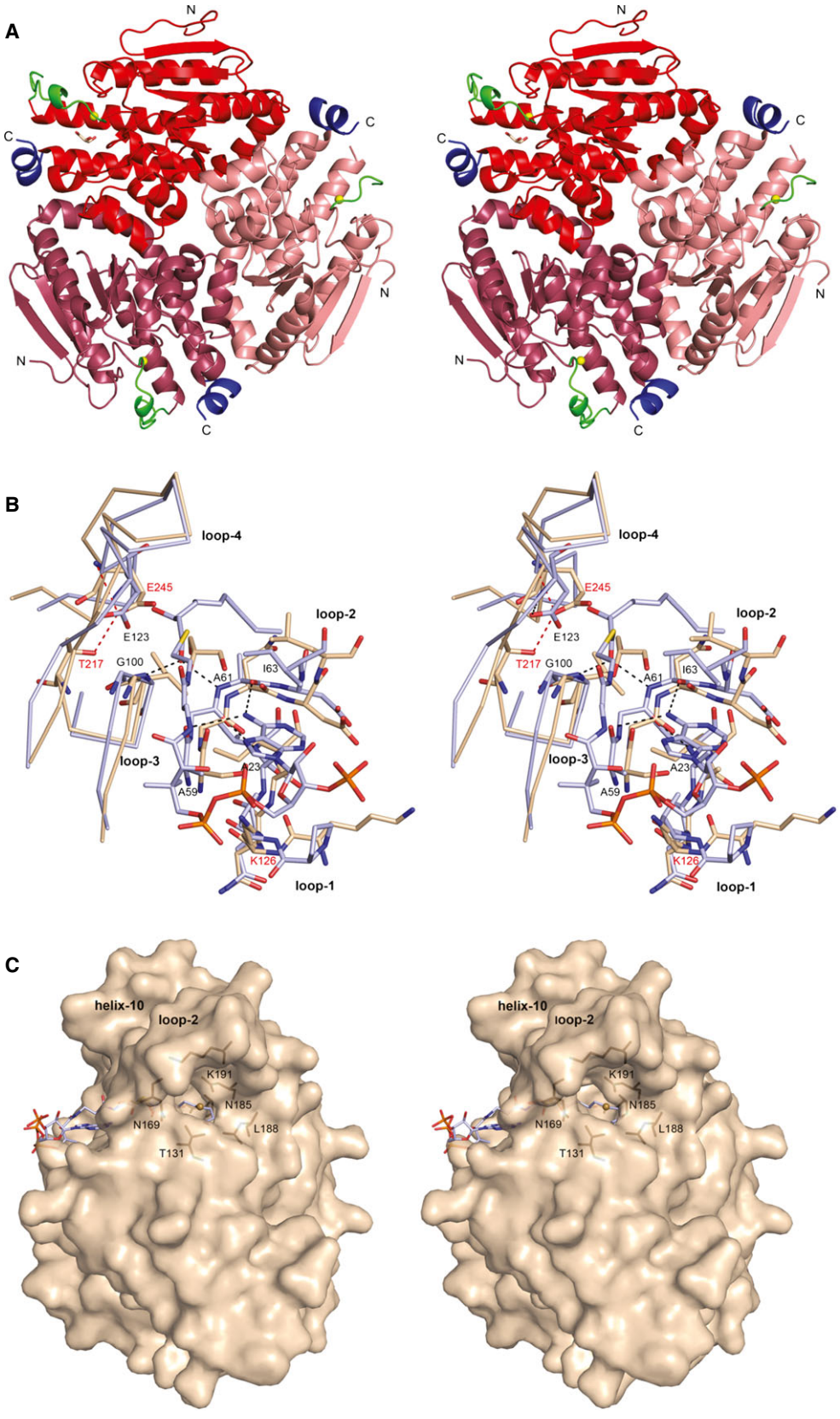
A
N
C
C
N
N
C
N
C
C
N
B
loop-4
E245
loop-2
E123
T217
G100
A61
I63
loop-3
A23
A59
K126
loop-1
loop-4
E245
loop-2
E123
T217
G100
A61
I63
loop-3
A23
A59
K126
loop-1
C
helix-10
loop-2
K191
N185
N169
L188
T131
helix-10
loop-2
K191
N185
N169
L188
T131

The active site geometry of ISO-ECI2

Glu245, the catalytic base, is well defined by its electron density. It adopts an unusual side chain conformation and it is hydrogen bonded to its own main chain, N(Glu245), and to OG1(Thr217) via its OE1 (Glu245) carboxylate oxygen (Fig. 6), whereas OE2 (Glu245) points to the catalytic cavity and is surrounded by the side chains of four hydrophobic residues: Leu189 (loop-2), Ile214 (helix-3), Phe237 (loop-4) and Leu335 (helix-9). Also in yeast ECI2 the catalytic glutamate Glu158 is hydrogen bonded to a side chain, Asn101 [11]. In the structure of ECI1 the flap region of loop-4 (residues Glu245-Gly246-Gly247-Cys248 in HsECI2) adopts a different conformation and in this subfamily of ECIs (Fig. 3B) the catalytic base Glu136 protrudes into the catalytic site out of a different position of loop-4 (Fig. 3) [8,9]. This position is the same as that of the catalytic glutamate Glu164 in the ECH structure (Fig. 3A), which is also proposed to exchange a proton with the C2 atom [31]. In the latter structure there are actually two glutamates. The second glutamate (Glu144) protrudes out of helix-3 and these two glutamates (Glu144 and Glu164) are both hydrogen bonded to the same catalytic water, which thereby becomes activated for nucleophilic attack to the double bond of the enoyl-CoA substrate, to achieve the chirally specific hydration of the double bond [32]. These two glutamates, protruding out of helix-3 and loop-4, are also present in MFE1, being Glu103 and Glu123 [16]. MFE1 is an efficient hydratase, which appears to be its main physiological function. The proposed MFE1 enoyl-CoA isomerase reaction mechanism, dependent on the catalytic water [16], is different from the reaction mechanisms of ECI1 [9] and ECI2 [18].

A comparison of the structures of ISO-ECI2 with MFE1 (3ZWC) and ECH (2DUB) suggests that the binding pocket for the tail will be shaped by loop-2. Indeed, in the ISO-ECI2 crystal structure a tunnel is present between the catalytic site and the bulk solvent, in each of the three subunits, allowing for fatty acyl tails of different chain lengths to bind (Fig. 6). This is in good agreement with the kinetic data for rat ECI2 [6] and the calorimetric data for HsECI2 (Table 2), showing that this ECI2 can use as substrate fatty acyl-CoAs with a broad range of fatty acyl chain lengths. Also in ECI1 the fatty acyl tail is bound in a tunnel, but in this subfamily the tunnel is shaped by loop-4 (Fig. 2). Figure 6 visualizes the ISO-ECI2 tunnel shaped by loop-2, in particular the side chains of residues Asn165, Asn169, Asn184, Leu188 and Leu189. Also contributing to this tunnel are the side chains of residues Thr131 and Tyr134 of loop-1, Ile214 of helix-3 and Trp340 of helix-9. Hydrophobic side chains such as Leu188 and Leu189 as well as polar side chains such as Tyr134 and Asn165 contribute to the tunnel. Also a water and a chloride ion are bound inside the tunnel (Fig. 6). The water is hydrogen bonded to Glu245 and the chloride ion contacts at a distance of about 5 Å this water and the side chains of Tyr134, Asn165, Asn185, Leu188, Leu189 and Trp340. Chloride ions were present in the crystallization buffer at a concentration of 100 mM. The rim of the tunnel is shaped by the side chains of Thr131, Asn169, Lys181, Asn185 and Leu188. The length of the tunnel measured from OE2(Glu245) to OG1(Thr131) is about 14 Å, which corresponds approximately to the length of an extended acyl tail of 12 carbon atoms.

Helix-10

The active site is covered by helix-10, which is the C-terminal helix (Fig. 2). The function of helix-10 in the crotonase superfamily has not yet been studied. It

Fig. 6. (A) The stereo view of the ISO-ECI2 trimer. The C-terminal helix-10 is in dark blue and the loop-2 is in green. The N terminus and the C terminus of each of the subunits are labeled with N and C, respectively. In stick model is shown the glycerol as bound to the active site of the A subunit. Chloride ions in each subunit are shown in yellow. (B) The structural comparison of the loops involved in binding and catalysis of ISO-ECI2 (brown) and the hydratase domain of MFE1 (3ZWC, light blue) (similar view as in Fig. 2, rotated somewhat about the horizontal direction). In ISO-ECI2 it concerns loop-1 (Lys125-Ile129), loop-2 (Ser163-Leu167), loop-3 (Pro210-Thr217) and loop-4 (Phe233-Ser248). In the ISO-ECI2 structure the active site glycerol is also shown, as a stick model. The mode of binding of the 3S-hydroxydecanoyl-CoA to the MFE1 hydratase active site shows that the adenine ring is wedged between Ala23 (loop-1) and Ile63 (loop-2). Black dotted lines mark the hydrogen bonds between the adenine amino group and O(Ala59) and O(Ala61) (loop-2). Also highlighted by black dotted lines are the hydrogen bonds between the thioester oxygen atom of 3S-hydroxydecanoyl-CoA and N(Ala61) (loop-2) and N(Gly100) (loop-3) and the hydrogen bond between loop-1 and loop-2 (Val24-Gly60) in the MFE1 complex. The hydrogen bonds anchoring the side chain of the catalytic Glu245 of ISO-ECI2 are shown by red dotted lines. In red is also shown Lys126 of loop-1 of ISO-ECI2 predicted to be important for substrate binding. (C) The tunnel of ISO-ECI2 which is predicted to bind the acyl moiety (subunit A, similar view to Fig. 2, stereo). The superimposed 3S-hydroxydecanoyl-CoA product of MFE1 hydratase (3ZWC) is shown as stick representation. The tunnel is formed by loop-2, loop-1, helix-3 and helix-9. The rim of the tunnel is formed by the side chains Thr131 (loop-1), Asn169 (loop-2), Lys181 (loop-2), Asn185 (loop-2), Leu188 (loop-2) (all shown as black sticks). Also visualized is the chloride ion bound in this tunnel (orange dot).

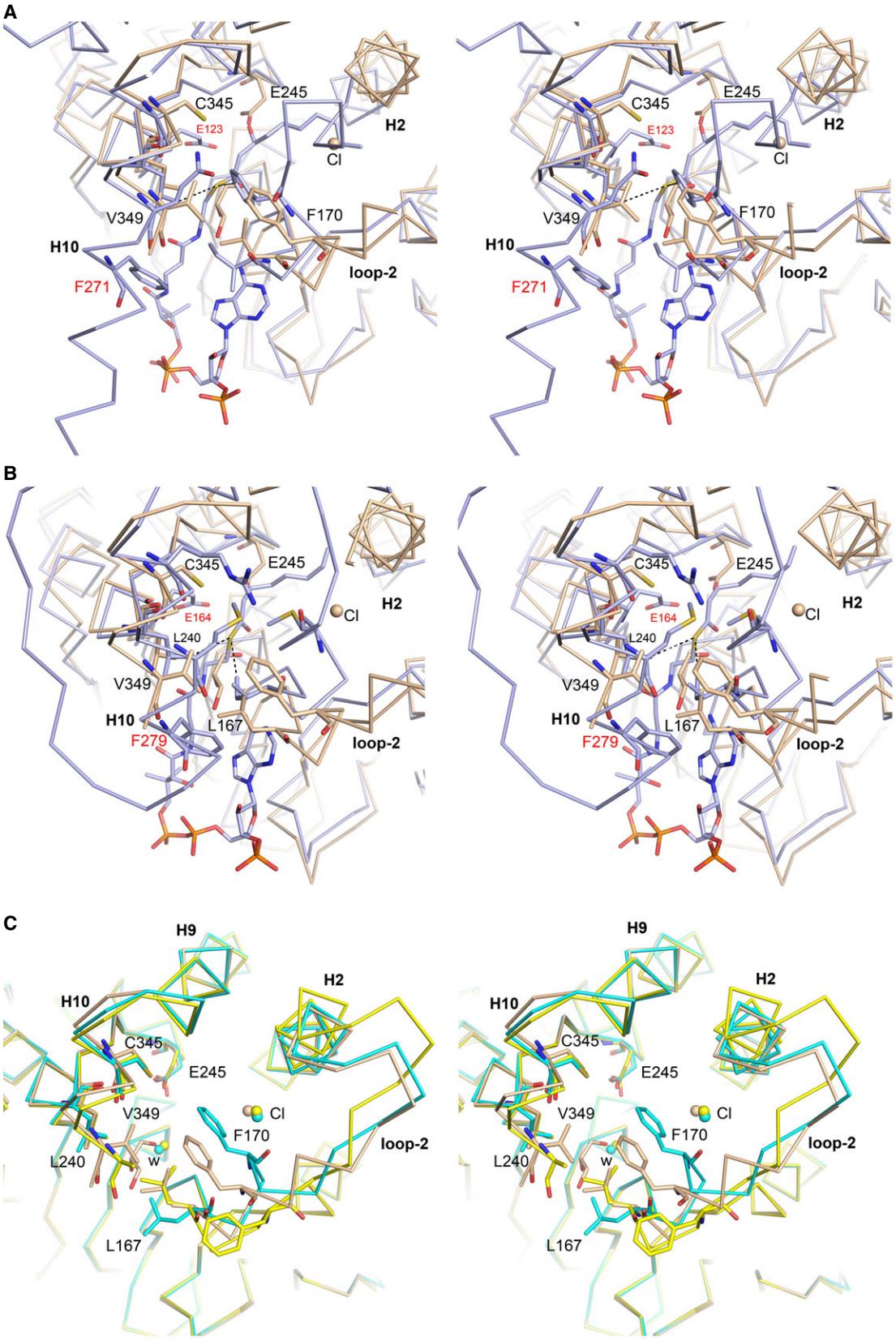
A
C345
E245
E123
H2
Cl
V349
F170
H10
loop-2
F271
B
C345
E245
H2
E164
Cl
L240
V349
H10
L167
F279
loop-2
C
H9
H2
H10
C345
E245
V349
Cl
F170
loop-2
L240
w
L167

appears to be involved in ligand binding interactions as at least one basic residue protruding out of helix-10 interacts with the phosphate moieties of the acyl-CoA substrate in the corresponding structures of these complexes. The presence of basic residues in helix-10 is seen in each of the sequences listed in Fig. 3. In addition, from the sequence (Fig. 3) and structural comparisons it can be noted that a second conserved feature of helix-10 concerns the presence of hydrophobic residues pointing inwards, towards a hydrophobic cluster of residues that covers the binding pocket of the ligand near the thioester moiety. In HsECI2 these residues are Cys345, Val349 and Phe352 (Figs 3 and 7). Other residues that contribute to this cluster are protruding out of loop-2 (Leu167 and Phe170) and loop-4 (Leu240). In Fig. 7 the hydrophobic interactions between helix-10 and loop-2 and loop-4 of ISO-ECI2 are compared with the corresponding geometry of the ECH and MFE1 structures. In ECH the corresponding residues are Arg272, Met276 and Phe279 of helix-10, Ile100 and Met103 of loop-2 and Leu167 of loop-4, and in MFE1 they are residues Ala264, Gln268 and Phe271 (helix-10), Ile63 and Phe66 (loop-2) and Leu126 (loop-4). It can be noted that Ile100 of ECH also contributes to the binding pocket for the adenine ring (Fig. 6). Ile100 is in van der Waals contact with the sulfur atom of the thioester moiety, like Phe66 in MFE1 (Fig. 7). The conserved leucine of loop-4 also contacts the sulfur of the thioester moiety in each of the liganded structures at a distance of approximately 4.0 Å. In HsECI2 Leu167 of loop-2 and Leu240 of loop-4 correspond to these hydrophobic residues of MFE1 and ECH.

The crystal structures of ISOA-ECI2 and ISOB-ECI2

The importance of Val349 and that of helix-10 for catalysis was investigated by the characterization of the V349A point mutation variant (ISOA-ECI2) and the helix-10 deletion variant (ISOB-ECI2), in which the C-terminal residues 350–355 were deleted (Fig. 3). These variants have somewhat lower stability than the wild-type ISO-ECI2 trimer (Fig. 4), but crystallization experiments with both variants yielded well-diffracting crystals.

The affinity of the two variants for acyl-CoA molecules with a saturated chain is somewhat higher compared to wild-type ISO-ECI2. For example, the K_d of decanoyl-CoA for ISO-ECI2, ISOA-ECI2 and ISOB-ECI2 is 37, 25 and 10 μM, respectively, as measured by calorimetry (Table 2). The enthalpy of binding of these substrate analogues to ISOA-ECI2 and ISOB-ECI2 is much higher than for binding to ISO-ECI2. For the ISOA-ECI2 variant, catalytic activity could be detected. In the presence of 100 μM 3E-hexenoyl-CoA and 3E-decenoyl-CoA, the activities are 2.5 and 9.2 $\mu mol \cdot min^{-1} \cdot mg^{-1}$, respectively, whereas for ISO-ECI2 these activities are 4.5 and 18.7 $\mu mol \cdot min^{-1} \cdot mg^{-1}$. For the helix-10 deletion mutant ISOB-ECI2, no catalytic activity could be detected with the 3E-hexenoyl-CoA and 3E-decenoyl-CoA substrates. Clearly, the C-terminal end of helix-10 is required for efficient catalysis.

The crystal structures of ISOA-ECI2 and ISOB-ECI2 were determined (Tables 4 and 5). In each structure, the asymmetric unit consists of a trimer, as in the wild-type crystals. Clearly, the mutation does not affect the trimerization of the subunits.

In ISOA-ECI2 helix-10 is disordered after the V349A residue in subunits A and C, but in subunit B it could be built up to residue Arg355, which is the C-terminal residue. This is a consequence of crystal packing, as the C-terminal part of helix-10 is stabilized by a neighboring molecule. Loop-2 of the ISOA-ECI2 is only well defined in subunit A, whereas the Phe170-Thr171-Asp172-Ile173 residues of subunits B and C were not modeled. In wild-type ISO-ECI2 the Leu167

Fig. 7. The hydrophobic cluster which anchors helix-10 to loop-2 and loop-4 of human ISO-ECI2 (light brown, subunit A) aligned with (A) the hydratase domain of MFE1 with bound 3S-hydroxydecanoyl-CoA (3ZWC, light blue) and (B) ECH with bound octanoyl-CoA (2DUB, light blue). The following side chains of the ISO-ECI2 crystal structure are shown: Leu167 and Phe170 of loop-2, Leu240 of loop-4, and Cys345 and Val349 of helix-10 (Phe352 of helix-10 is not ordered in this subunit). The glycerol molecule in the active site of ISO-ECI2 and the chloride ion in the hydrophobic tunnel are also shown as light brown sticks and yellow sphere, respectively. Also shown in each of the panels is the loop-4 catalytic glutamate, being Glu245 in ECI2-ISO, Glu123 in MFE1 and Glu164 in ECH. In (A) the corresponding hydrophobic residues of MFE1 are Ile63, Phe66, Leu126, Ala264, Gln268 and Phe271. In (B) the corresponding residues of ECH are Ile100, Met103, Leu167, Arg272, Met276, Phe279. The van der Waals interactions between the sulfur atom of the acyl-CoA ligand and the side chains of Phe66, Leu126 (in MFE1) and Ile100, Leu167 (in ECH) are highlighted by black dotted lines (the corresponding residues in ISO-ECI2 are Leu167, Leu240 respectively). (C) Superposition of ISO-ECI2 (light brown) with ISOA-ECI2 (yellow) and ISOB-ECI2 (cyan), highlighting the loop-2 changes of Phe170 (in ISOA-ECI2 and ISOB-ECI2) and Leu167 (in ISOB-ECI2). View obtained by rotating around the horizontal direction with respect to (A) and (B); similar view as in Fig. 2. Key residues of loop-2, loop-4 and helix-10 are shown and labeled. Also shown is the glycerol molecule bound in the OAH of ISO-ECI2 and the corresponding OAH waters in ISOA-ECI2 and ISOB-ECI2. The catalytic glutamate (Glu245) and the chloride ion of each of the three structures are shown and labeled.

and Phe170 side chains of loop-2 are in van der Waals contact with the Val349 side chain, but in subunit A of ISOA-ECI2 the Phe170 side chain points towards the bulk solvent whereas the Leu167 conformation does not change (Fig. 7). In ISOB-ECI2, helix-10 can be built up to residue Thr346 in subunit C and up to residue Cys345 in subunits A and B. Loop-2 adopts a defined and similar conformation in each of the three subunits. It is best defined in subunit C. The Phe170 side chain points further inwards and Leu167 points further outwards, compared to the wild-type enzyme.

Although the mutational differences of ISOA-ECI2 and ISOB-ECI2 concern the helix-10 sequence, there are no structural changes in this helix. There are also no structural changes at the catalytic site, near Glu245, or in the fatty acyl tail binding tunnel, where the chloride ion binding site is also preserved in ISOA-ECI2 and ISOB-ECI2 (Fig. 7). There are structural differences in loop-2, however, in particular in ISOB-ECI2 (Fig. 7). These structural differences correlate with differences in catalytic properties, including the lower specific activity of ISOA-ECI2 and no catalytic activity of ISOB-ECI2, although calorimetric data for both variants show that they still bind the longer saturated substrate analogues tightly (Table 2). In ISOB-ECI2, loop-2 becomes more rigid in each of the three subunits and the Phe170 side chain points further inward, towards the fatty acyl binding tunnel, and it is in van der Waals contact with the chloride ion that is bound in this tunnel. In this inward pointing position, the Phe170 side chain would not block the tunnel, allowing for binding of saturated substrate analogues (as detected by calorimetry). In its new position, the Phe170 side chain has moved into an empty space, which in ISO-ECI2 connects the catalytic site to bulk solvent. This somewhat narrow exit tunnel between catalytic site and bulk solvent, defined by loop-2 (Phe170, Lys181, Asn185), loop-4 (Gln242) and helix-9 (Trp340), is visualized in Fig. 8. The possible functional role of this alternative exit tunnel for binding of the fatty acyl tails is not clear. In any case, it identifies an alternative exit path for binding the fatty acyl tail (between helix-9 and helix-2), which is different from the exit tunnel in ECI1 (between loop-4 and helix-9; Fig. 2) and from the MFE1 exit path (between helix-2 and loop-1/helix-1) (Figs 2 and 6). In ECH the exit path for the fatty acyl tail is made by unfolding of helix-2 [17]. Possibly more important for catalysis is the movement of Leu167 of the hydrophobic cluster away from the thioester moiety. This conserved hydrophobic cluster and the catalytic base are on opposite sides of the thioester moiety: the cluster effectively shields the reactive thioester moiety from bulk solvent (Figs 7 and 8). In the mutated variants the positions of Leu167 (in ISOB-ECI2) and Phe170 (in ISOA-ECI2 and ISOB-ECI2) change (Fig. 8). In particular, in ISOB-ECI2, being inactive, these structural changes possibly affect the correct positioning of the thioester moiety in its binding pocket. These results therefore suggest that the function of this hydrophobic cluster could be to fix the reactive thioester moiety rigidly in its binding pocket. This tight binding then ensures that the thioester oxygen binds correctly in its OAH allowing for optimal stabilization of the enolate intermediate when it is formed in the catalytic cycle, facilitating efficient catalysis.

Concluding remarks

Our SAXS data indicate that the ACBP domains are placed at the periphery of the isomerase trimer, extending the flat shape of the trimer (Fig. 5). Hence, the full-length isomerase is a highly flattened trimer, with all domains in the same plane. The structure directly suggests that there is no cross-talk between the ACBP domains from different chains. The ACBP domains have high affinity towards saturated acyl-CoA molecules (which are substrate analogues) for both short- and long-chain acyl moieties, whereas for the isomerase domain the affinity depends much more on the length of the acyl moiety, being significantly lower for short-chain acyl-CoA ligands (Table 2). For short/medium-chain substrates, like 3E-hexenoyl-CoA and 3E-decenoyl-CoA, the k_{cat}/K_m values of FL-ECI2 are higher than those for ISO-ECI2 (Table 1), suggesting that the ACBP domain is important for efficient metabolism of short/medium-chain 3E-enoyl-CoA substrates. The HsECI2 crystal structures suggest that the fatty acyl tails of the enoyl-CoA substrates bind in a tunnel accommodating medium-chain as well as long-chain fatty acyl tails. This tunnel extends from the catalytic site to bulk solvent and is mainly shaped by residues of loop-2 and loop-1. Structural comparisons show that the OAH geometry is a strictly conserved feature of the catalytic site of this group of enzymes, whereas the catalytic glutamate can protrude into the catalytic cavity from different positions in loop-4. Also the fatty acyl tail binding tunnel is shaped in various ways by the loops following after the β-strands of sheet B. In several structures of the subfamily of hydratases and isomerases of the crotonase superfamily, the C-terminal part of helix-10 is disordered, in particular in unliganded structures, but our mutagenesis studies clearly show the importance of helix-10 for catalysis. These studies highlight also the importance of loop-2. It remains intriguing that ECI2 can isomerize both 3Z- and 3E-enoyl-CoA

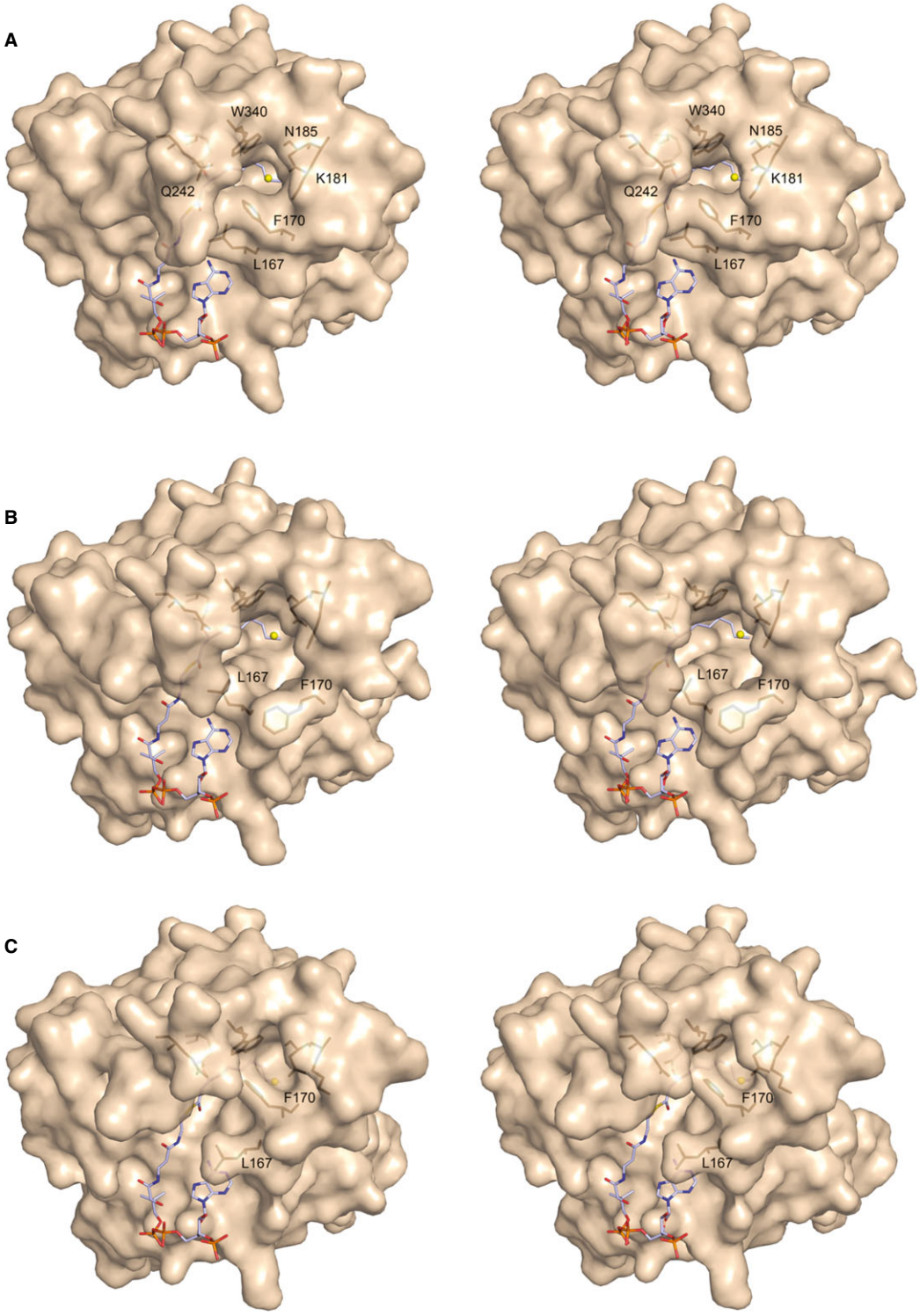

Fig. 8. Surface representation of the crystal structures of (A) ISO-ECI2 subunit A, (B) ISOA-ECI2 subunit A and (C) ISOB-ECI2 subunit C showing the narrow exit tunnel from the catalytic site. The view is similar to Fig. 7. The residues lining this tunnel in ISO-ECI2, Phe170, Lys181, Asn185 (of loop-2), Gln242 (loop-4) and Trp340 (loop-9), are labeled in (A). Also labeled in each of the panels are Leu167 and Phe170 of loop-2. Catalytic glutamate (not labeled) is faintly visible behind Gln242. Each structure has the chloride ion bound to the wider exit tunnel (not visible in the ISOB-ECI2 structure in C). A 3S-hydroxyacyl-CoA molecule, as bound to the MFE1 active site, is shown in each panel. The tail of this molecule fits well into the wider exit tunnel of HsECI2.

substrates. The presence of the main tunnel (defined by loop-2 and loop-1) and the narrower exit tunnel (defined by loop-2 and loop-4) in ISO-ECI2 might be relevant for its substrate specificity. Further crystallographic binding studies with ISO-ECI2, aimed at a better understanding of the role of loop-2 for substrate specificity, have been initiated.

Materials and methods

Site-directed mutagenesis and protein expression

For the expression of the FL-ECI2, ISO-ECI2 and ACBP-ECI2 constructs, the plasmids Pet28a-FL-ECI2 (residues Met1-Leu359), PNIC28-Bsa4-ISO-ECI2 (Gly103-Arg355) and Pet28a-ACBP-ECI2 (Met1-Ser89) were used, respectively. The FL-ECI2 and ACBP-ECI2 plasmids (provided by J. Knudsen) contained an N-terminal purification tag with a thrombin cleavage site (MGSSHHHHHHSSGLV PRGSHMASSQST)) before Met1 (Fig. 3), while the ISO-ECI2 plasmid (obtained from the Structural Genomics Consortium (SGC), Oxford, UK) contained an N-terminal $(His)_6$-tag followed by a TEV protease cleavage site (MHHHHHHSSGVDLGTENLYFQS). The ISO-ECI2 plasmid was also used as a template for mutagenesis to prepare the helix-10 variants ISOA-ECI2 and ISOB-ECI2. Mutagenesis was performed with the QuikChange site-directed mutagenesis kit (Agilent Technologies, Santa Clara, CA, USA) using the forward primers 5′-CAGA TGAATGCACAAATGCT**GCA**GTGAACTTCTTATCC-3′ (ISOA-ECI2) and 5′-CAGATGAATGCACAAATGCT GTG**TGA**CAGTAAAGGTGGATACGG-3′ (ISOB-ECI2) and the reverse primers 5′-GGATAAGAAGTTCAC**TGC** AGCATTTGTGCATTCATCTG-3′ (ISOA-ECI2) and 5′-CCGTATCCACCTTTACTG**TCA**CACAGCATTTGTGCA TTCATCTG-3′ (ISOB-ECI2) (the mutation sites are shown in bold).

The FL-ECI2 and ACBP-ECI2 plasmids were transformed into BL21(DE3) cells, whereas the ISO-ECI2, ISOA-ECI2 and ISOB-ECI2 plasmids were transformed into BL21 (DE3)pLysS competent cells. The expression of recombinant proteins was performed in 1 L M9ZB medium (1% N-Z case plus® casein hydrolysate, 85 mM NaCl, 20 mM NH_4Cl, 20 mM NaH_2PO_4, 1 mM $MgSO_4$, 0.4% glucose) containing 30 $\mu g \cdot mL^{-1}$ kanamycin and 34 $\mu g \cdot mL^{-1}$ chloramphenicol. The culture was grown at 37 °C at 200 r.p.m. until an A 600 of 0.6 was reached, and protein expression was initiated with IPTG using a final concentration of 0.5 mM (for ISOA-ECI2 and ISOB-ECI2) or 1 mM (for FL-ECI2, ISO-ECI2 and ACBP-ECI2). After an overnight expression at 18 °C, the cells were collected using centrifugation and resuspended in the lysis buffer (Table 4). At the end, the cell suspensions were stored at −70 °C until further use.

Protein purification

The same general purification strategy was adopted for all constructs. The compositions of the purification buffers used for the crystallization studies are shown in Table 4. The cell pellet in lysis buffer was thawed and more lysis buffer was added to give a final volume of 40 mL per 1 L original culture. Lysis was enhanced by adding DNase1, RNaseA, lysozyme and $MgSO_4$ to the thawed cell suspension to a final concentration of 20 $\mu g \cdot mL^{-1}$, 2 $\mu g \cdot mL^{-1}$, 100 $\mu g \cdot mL^{-1}$ and 1 mM, respectively. The mixture was incubated at room temperature (40 min) under constant stirring and subsequently the soluble fraction was harvested by centrifugation (35 000 ***g***, 1 h). The clear supernatant was then passed through a Talon column equilibrated with the lysis buffer. The recombinant enzymes bound to the column were eluted with 250–500 mM imidazole (Table 4). The fractions containing the eluted protein were concentrated using either a 3 kDa (for ACBP-ECI2) or a 10 kDa cut-off centrifugal filter (for the FL-ECI2, ISO-ECI2, ISOA-ECI2, ISOB-ECI2). In the next step, the enzymes were passed through the Hiload 16/60 Superdex 200 Prep Grade gel filtration column using an Äkta Purifier purification unit (GE Healthcare, Uppsalla, Sweden). The fractions containing the recombinant protein were pooled, concentrated and stored in small quantities at −70 °C in the gel filtration buffer (Table 4). The enzyme concentration was determined by UV absorption, using extinction coefficients of 34 295, 19 940 and 15 470 $M^{-1} \cdot cm^{-1}$ for FL-ECI2, ISO-ECI2 (and helix-10 variants) and ACBP-ECI2, respectively. The storage buffer for the FL-ECI2, ISO-ECI2 and ACBP-ECI2 used for isothermal titration calorimetry (ITC) and kinetic experiments was 30 mM Tris/HCl, pH 8.5.

Static light scattering (SLS)

The oligomeric state of FL-ECI2 and ISO-ECI2 in solution was determined using SLS in the presence of 30 mM potassium phosphate buffer, pH 7.5. Approximately 50 μL of purified protein (4 $mg \cdot mL^{-1}$) was loaded onto a Superdex200 10/300 GL gel filtration column using an Äkta Purifier (GE Healthcare) and subsequently passed through a Shodex refractive index detector (for measuring the protein concentration) and a miniDAWN TREOS SLS instrument (Wyatt, Santa Barbara, CA, USA). The results were analyzed with ASTRA 5.3 (Wyatt).

Circular dichroism (CD) and thermal denaturation

For CD measurements the protein was diluted to 30 $\mu g \cdot mL^{-1}$ using 30 mM potassium phosphate, pH 7.5. The wavelength range used was 190–260 nm at a temperature of 20 °C. The cuvette path length was 0.1 cm. Thermal denaturation was carried out from 20 to 90 °C using a temperature ramp of 1 $°C \cdot min^{-1}$. The instrument used was the

Applied Photophysics Chirascan™, Surrey, UK. For all measurements, buffer spectra were subtracted to give the enzyme spectrum. For data analysis the wavelength range used was 200–240 nm. T_m values were calculated with GLOBAL3 (Applied Photophysics) by curve fitting calculations using the spectral changes as a function of temperature. A two-transition unfolding model for ECI2-FL was used (predicting the T_m value of the intermediate to be 54.3 ± 1.4 °C), whereas for ISO-ECI2, ACBP-ECI2, ISOA-ECI2 and ISOB-ECI2 a one-transition unfolding model was used.

Substrate synthesis

Acyl-CoA thioesters were prepared by the mixed anhydride method [33] and purified on reverse phase silica gel (RP-18; ICN Chemicals, Costa Mesa, CA, USA). The substrates were verified by determining their masses using an ESI-FTICR mass spectrometer (APEX II; Bruker, Bremen, Germany).

Enzyme activity measurements

Enzyme activities were determined by monitoring the formation of NADH spectrophotometrically at 340 nm in a coupled assay. The measurements were done in 50 mM Tris/HCl, pH 8.5, and the final assay mixture (0.5 mL) was composed of 1 mM NAD^+, 25 ng (FL-ECI2) or 50 ng (ISO-ECI2 and its variants) of enzyme and 5–300 μM substrate. In addition, 1.6 μg of *Drosophila melanogaster* multifunctional enzyme type 2 (DmMFE2) was used in the assays as a linker enzyme. This linker enzyme was purified as previously described [34] with little modification. The substrate concentration was determined by the Ellman test [35]. The measurements were carried out with the Jasco V-660 spectrophotometer (Jasco Inc., Easton, PA, USA). In all experiments the reaction components were allowed to equilibrate at room temperature for about 10 min before starting the reaction by adding the substrate. NADH formation was monitored for 3 min by observing the change in absorbance at 340 nm. The extinction coefficient of 6220 $M^{-1}\cdot cm^{-1}$ was used for the conversion calculations. All experiments were performed at 25 °C and were done at least in duplicate. The data were fitted to the Michaelis–Menten equation using GRAPHPAD PRISM software (GraphPad Software Inc., La Jolla, CA, USA).

Isothermal titration calorimetry (ITC)

ITC experiments were done with protein solutions in 30 mM Tris/HCl, pH 8.5. The saturated fatty acyl-CoA powder (Sigma, Helsinki, Finland) was dissolved in the same buffer. Ligand concentrations were determined using Ellman's test. Before each experiment the protein samples were degassed at 25 °C for 8–16 min using the ThermoVac instrument (GE Healthcare). ITC experiments were performed with a MicroCal ITC200 calorimeter (GE Healthcare). Temperature equilibration was carried out for 15–20 min before each experiment. The sample cell was filled with 200 μL of the enzyme (40–180 μM as calculated for the subunit or monomer), the protein concentrations being dependent on the protein construct. A total of 38 μL of ligand solution (1–3.9 mM) using 1 μL per injection into the sample cell was used. The time between each injection was 120 s, with an initial delay of 60 s before the first injection. For titration of ISO-ECI2 with octanoyl-CoA, two data files were combined using the CONCAT software (MicroCal) since saturation could not be reached with one measurement. All experiments were carried out at 25 °C under constant stirring at 500 r.p.m. Data analysis and curve fitting were carried out using ORIGIN 7.0 (MicroCal).

Small angle X-ray scattering

Synchrotron SAXS data were collected on beamline I911-4 at MAX-Lab (Lund, Sweden) and beamline P12 at PETRA III, EMBL/DESY (Hamburg, Germany). For FL-ECI2 (2.2 $mg\cdot mL^{-1}$), the SAXS data were measured in the presence and absence of acyl-CoA ligands, including octanoyl-, decanoyl- and lauroyl-CoA at 50–200 μM. SAXS measurements were also carried out for ISO-ECI2 (4.1 $mg\cdot mL^{-1}$) and ACBP-ECI2 (5.7 $mg\cdot mL^{-1}$) in the absence of ligands. Exposure times were 2 min at I911-4 (λ = 0.91 Å) and 20 × 50 ms at P12 (λ = 1.24 Å). The corresponding buffers (FL-ECI2, 30 mM Tris, pH 8.5; ISO-ECI2 and ACBP-ECI2, 30 mM HEPES, pH 7.5, 100 mM NaCl) were similarly measured, and buffer contribution was subtracted from the protein data. For each sample a 50% dilution was also measured, and for all modeling runs data merged from the two concentrations were used. The exception was the full-length protein, which always aggregated in the X-ray beam to some extent when it had been diluted. Hence, only the highest concentration was used for analyses of FL-ECI2, and no aggregation was evident in linear Guinier plots.

Programs of the ATSAS package [36] were used for data processing and analysis. Distance distributions were calculated using GNOM [37], and *ab initio* models were built using DAMMIF [38] and GASBOR [39]. Hybrid modeling employing rigid body refinement and loop building for FL-ECI2 was done with CORAL [36] and BUNCH [40], respectively. The model was created using 3-fold symmetry and the crystal structure of ISO-ECI2 (2F6Q; SGC, Oxford, UK), represented the isomerase domain (corresponding to residues Thr106-Asn347) and the NMR structure of the HsECI2 ACBP domain (2CQU, corresponding residues Ser4-Ser84). Structure superpositions were done using SUPCOMB [41]. Theoretical SAXS data for crystal structures were calculated with CRYSOL [42].

Crystallization and data collection

Crystallization was performed using 96-well plates and the sitting-drop vapor diffusion method. Crystallization drops were prepared by the Mosquito crystallization robot (TTP Labtec, Melbourn, UK) by mixing 0.5 μL of the protein solution with 0.5 μL well solution (Table 4). The plates were incubated at room temperature and imaged using the Formulatrix RI54 plate hotel. ISO-ECI2 (5.2 $mg{\cdot}mL^{-1}$, supplemented with 0.5 mM decanoyl-CoA in the protein solution) crystallized in 100 mM MES pH 6.5, 1 M $(NH_4)_2SO_4$, and the crystals grew to their maximum size in 6–10 days. ISOA-ECI2 (4.1 $mg{\cdot}mL^{-1}$, protein solution supplemented with 0.5 mM lauroyl-CoA) and ISOB-ECI2 (3.5 $mg{\cdot}mL^{-1}$) were crystallized and cryo-cooled in different conditions but using the same protocol as described for ISO-ECI2 (Table 4). Before data collection, the crystals were briefly passed through the crystallization mother liquor, supplemented with 20% glycerol and a ligand (Table 4), and subsequently cryo-cooled in liquid nitrogen. Data collection was carried out on the ID29 beam line at ESRF (Grenoble, France) and on the beam line I03 of the Diamond Light Source (DLS), Oxford, UK (Table 5). Data processing was carried out using XDS [43]. Scaling was carried out using XSCALE [43] or AIMLESS [44] of the CCP4 suite [45]. The data processing statistics are listed in Table 5.

Structure determination, model building and refinement

The determination of the three structures was done by molecular replacement using PHASER [46]. The structure of the ISO-ECI2 construct (2F6Q), without ligands, was used as the search model for all three structure determinations. There are three subunits per asymmetric unit in each structure. Refinement was carried out using REFMAC5 [47] and iterative cycles of model building were done using COOT [48]. The REFMAC5 refinement was carried out using non-crystallographic symmetry restraints. The refinement was finalized when no significant peaks were found in the $F_o - F_c$ map. The models obtained have good refinement statistics and geometry (Table 5).

Structure and sequence analysis

There is good electron density for most of the residues, except for some residues of loop-2 which have high *B*-factors in most of the chains, in particular residues Phe170-Thr171-Asp172-Ile173. Also the residues at the N terminus and C terminus in most chains are disordered. The Ramachandran plot calculated by MOLPROBITY [49] shows few outliers in the flexible loops. The only outlier, which is built in well defined density, is Ser257, adopting φ/ψ values of approximately 75°/125° in each of the three chains of each of the models.

A complete trace was built for subunit A of the ISO-ECI2 structure (from residue Gly103; also present is Met102 plus seven additional N-terminal tag residues); for this subunit loop-2 is defined and it has the same conformation as in subunit C. For subunit B the loop-2 residues Phe170-Val178 of loop-2 could not be built. The C-terminal residues are Val350 for each of the subunits. For ISOA-ECI2, the trace of subunit B starts at Met102, the C-terminal helix-10 is ordered and the V349A mutation is clearly visible in the map. However, for this subunit loop-2 residues Phe170-Thr171-Asp172-Ile173 could not be built due to its intrinsic disorder; these residues are only well defined in subunit A. The C-terminal residues are Ala349, Arg355 and Ala348 for, respectively, subunits A, B and C. For the ISOB-ECI2 structure a complete trace could be built for subunit C from Gly103 to Thr346; also Met102 was built plus five additional N-terminal tag residues. For ISOB-ECI2 loop-2 could be built for each of the three subunits, having the same conformation; it is best defined in subunit C. The C-terminal residues are Cys345, Cys345 and Thr346 for respectively subunits A, B and C.

The crystal structure ISO-ECI2 (2F6Q) which has been used for the molecular replacement calculation is an unliganded complex of the SeMet derivative of the ISO-ECI2 construct of HsECI2, crystallized in 0.1 M Tris, pH 8.5, in the presence of 20% isopropanol. In this crystal structure loop-2 is also a high *B*-factor loop except in subunit B for which the loop-2 conformation was built in a similar conformation as in the ISO-ECI2 subunit A structure. Crystal structures of rat peroxisomal MFE1 (3ZWC) [16], rat mitochondrial ECH (2DUB) [17], mitochondrial ECI1 of human (1SG4) [9] and rat (1XX4) [8], rat mitochondrial DECI (1DCI) [50] and yeast (*S. cerevisiae*) peroxisomal ECI2 (1PJH) [11] were also used in the comparison studies. The structures of ACBP used for structural analysis were the NMR structures of the bovine ACBP (1ACA) [30] complexed with palmitoyl-CoA and the human ACBP-ECI2 domain (2CQU) as well as the crystal structures of human (2CB8, complexed with myristoyl-CoA, and 2FJ9, unliganded) [22] and *Plasmodium falciparum* ACBP, complexed with myristoyl-CoA (1HBK) [29]. The sequence alignment of human ECI2 with homologous enzymes was performed using CLUSTALW2 [51] on the EBI server (http://www.ebi.ac.uk/Tools/msa/clustalw2/). The sequence alignment was improved by structure superpositions carried out using the SSM [52] tool in COOT [48]. The secondary structure assignment was carried out using DSSP [53] from the CMBI server (http://www.cmbi.ru.nl/dssp.html). Evolutionary history was inferred using the neighbor-joining method, using MEGA5 [54]. The evolutionary distances were computed using the Poisson correction method and are in units of number of amino acid substitutions per site. The figures of the structures were prepared using PYMOL (http://www.pymol.org).

Acknowledgements

We thank Dr Jens Knudsen for the plasmids of FL-ECI2 and ACBP-ECI2. The plasmid of ISO-ECI2 was obtained from the SGC (Oxford, UK). The research leading to these results has received funding from the European Community's Seventh Framework Programme (FP7/2007-2013) under BioStruct-X (grant agreement no. 283570) and from the Academy of Finland (243008921). We thank Ville Ratas and Tiila Kiema for skillfully maintaining our BCO protein crystallography facility and Piotr Prus for help with the CD and ITC experiments. We gratefully acknowledge the expert support from the beam line scientists of the SAXS beam lines I911-4 (MAXlab, Lund, Sweden) and P12 (DESY, EMBL Hamburg, Germany) and the MX beam lines I03 (DLS, Oxford, UK) and ID29 (ESRF, Grenoble, France). We thank Petri Pihko for stimulating discussions on the crotonase catalytic properties, Tuomo Glumoff for providing the DmMFE2 plasmid, and Natalia Markova and Prasad Kasaragod for expert discussions on the ITC and enzyme kinetics data, respectively.

Author contributions

GUO performed the mutation, overexpression, purification, enzyme kinetics, calorimetric studies, crystallization, X-ray data collection, structure determination and SAXS sample preparation. MKK has been involved in crystal handling, data collection, data processing, structure analysis as well as with preparing the manuscript. RKW conceived and supervised the project while GUO contributed to the experimental design. PK performed the SAXS data collection and analysis. WS synthesized the substrates. GUO, MKK and RKW analyzed the structures and wrote the paper. All authors finalized the paper.

References

1 Van Weeghel M, Te Brinke H, van Lenthe H, Kulik W, Minkler PE, Stoll MS, Sass JO, Janssen U, Stoffel W, Schwab KO *et al.* (2012) Functional redundancy of mitochondrial enoyl-CoA isomerases in the oxidation of unsaturated fatty acids. *FASEB J* **26**, 4316–4326.

2 Hiltunen JK & Qin Y (2000) β-oxidation strategies for the metabolism of a wide variety of acyl-CoA esters. *Biochim Biophys Acta* **1484**, 117–128.

3 Miinalainen IJ, Schmitz W, Huotari A, Autio KJ, Soininen R, Ver Loren van Themaat E, Baes M, Herzig KH, Conzelmann E & Hiltunen JK (2009) Mitochondrial 2,4-dienoyl-CoA reductase deficiency in mice results in severe hypoglycemia with stress intolerance and unimpaired ketogenesis. *PLoS Genet* **5**, e1000543.

4 Janssen U & Stoffel W (2002) Disruption of mitochondrial β-oxidation of unsaturated fatty acids in the 3,2-trans-enoyl-CoA isomerase-deficient mouse. *J Biol Chem* **277**, 19579–19584.

5 Gurvitz A, Mursula AM, Firzinger A, Hamilton B, Kilpeläinen SH, Hartig A, Ruis H, Hiltunen JK & Rottensteiner H (1998) Peroxisomal Δ^3-*cis*-Δ^2-*trans*-enoyl-CoA isomerase encoded by ECI1 is required for growth of the yeast *Saccharomyces cerevisiae* on unsaturated fatty acids. *J Biol Chem* **273**, 31366–31374.

6 Zhang D, Yu W, Geisbrecht BV, Gould SJ, Sprecher H & Schulz H (2002) Functional characterization of Δ^3, Δ^2 -enoyl-CoA isomerases from rat liver. *J Biol Chem* **277**, 9127–9132.

7 Van Weeghel M, Ofman R, Argmann CA, Ruiter JP, Claessen N, Oussoren SV, Wanders RJ, Aten J & Houten SM (2014) Identification and characterization of Eci3, a murine kidney-specific Δ3, Δ2 -enoyl-CoA isomerase. *FASEB J* **28**, 1365–1374.

8 Hubbard PA, Yu W, Schulz H & Kim JJ (2005) Domain swapping in the low-similarity isomerase/hydratase superfamily: the crystal structure of rat mitochondrial Δ^3, Δ^2 -enoyl-CoA isomerase. *Protein Sci* **14**, 1545–1555.

9 Partanen ST, Novikov DK, Popov AN, Mursula AM, Hiltunen JK & Wierenga RK (2004) The 1.3 Å crystal structure of human mitochondrial Δ^3, Δ^2 -enoyl-CoA isomerase shows a novel mode of binding for the fatty acyl group. *J Mol Biol* **342**, 1197–1208.

10 Kasaragod P, Venkatesan R, Kiema TR, Hiltunen JK & Wierenga RK (2010) Crystal structure of liganded rat peroxisomal multifunctional enzyme type 1: a flexible molecule with two interconnected active sites. *J Biol Chem* **285**, 24089–24098.

11 Mursula AM, Hiltunen JK & Wierenga RK (2004) Structural studies on Δ^3, Δ^2 -enoyl-CoA isomerase: the variable mode of assembly of the trimeric disks of the crotonase superfamily. *FEBS Lett* **557**, 81–87.

12 Holden HM, Benning MM, Haller T & Gerlt JA (2001) The crotonase superfamily: divergently related enzymes that catalyze different reactions involving acyl coenzyme a thioesters. *Acc Chem Res* **34**, 145–157.

13 Hamed RB, Batchelar ET, Clifton IJ & Schofield CJ (2008) Mechanisms and structures of crotonase superfamily enzymes-how nature controls enolate and oxyanion reactivity. *Cell Mol Life Sci* **65**, 2507–2527.

14 Engel CK, Mathieu M, Zeelen JP, Hiltunen JK & Wierenga RK (1996) Crystal structure of enoyl-coenzyme A (CoA) hydratase at 2.5 Å resolution: a

spiral fold defines the CoA-binding pocket. *EMBO J* **15**, 5135–5145.
15 Benning MM, Taylor KL, Liu R-Q, Yang G, Xiang H, Wesenberg G, Dunaway-Mariano D & Holden HM (1996) Structure of 4-chlorobenzoyl coenzyme A dehalogenase determined to 1.8 Å resolution: an enzyme catalyst generated via adaptive mutation. *Biochemistry* **35**, 8103–8109.
16 Kasaragod P, Schmitz W, Hiltunen JK & Wierenga RK (2013) The isomerase and hydratase reaction mechanism of the crotonase active site of the multifunctional enzyme (type-1), as deduced from structures of complexes with 3S-hydroxy-acyl-CoA. *FEBS J* **280**, 3160–3175.
17 Engel CK, Kiema TR, Hiltunen JK & Wierenga RK (1998) The crystal structure of enoyl-CoA hydratase complexed with octanoyl-CoA reveals the structural adaptations required for binding of a long chain fatty acid-CoA molecule. *J Mol Biol* **275**, 859–847.
18 Mursula AM, Van Aalten DM, Hiltunen JK & Wierenga RK (2001) The crystal structure of Δ^3, Δ^2 -enoyl-CoA isomerase. *J Mol Biol* **309**, 845–853.
19 Pihko P, Rapakko S & Wierenga RK (2009) Oxyanion holes and their mimics. In Hydrogen Bonding in Organic Synthesis (Pihko P, ed.), pp. 43–71. Wiley-VCH Verlag GmbH & Co. KGaE, Weinheim, Germany.
20 Papai I, Hamza A, Pihko PM & Wierenga RK (2011) Stereoelectronic requirements for optimal hydrogen-bond-catalyzed enolization. *Chemistry* **17**, 2859–2866.
21 Bach RD, Thorpe C & Dmitrenko O (2002) C–H···carboxylate oxygen hydrogen bonding in substrate activation by acyl-CoA dehydrogenases: synergy between the H-bonds. *J Phys Chem B* **106**, 4325–4335.
22 Taskinen JP, van Aalten DM, Knudsen J & Wierenga RK (2007) High resolution crystal structures of unliganded and liganded human liver ACBP reveal a new mode of binding for the acyl-CoA ligand. *Proteins* **66**, 229–238.
23 Antonenkov VD, Van Veldhoven PP, Waelkens E & Mannaerts GP (1997) Substrate specificities of 3-oxoacyl-CoA thiolase A and sterol carrier protein 2/3-oxoacyl-CoA thiolase purified from normal rat liver peroxisomes. Sterol carrier protein 2/3-oxoacyl-CoA thiolase is involved in the metabolism of 2-methyl-branched fatty acids and bile acid intermediates. *J Biol Chem* **272**, 26023–26031.
24 Koski KM, Haapalainen AM, Hiltunen JK & Glumoff T (2005) Crystal structure of 2-enoyl-CoA hydratase-2 from human peroxisomal multifunctional enzyme type-2. *J Mol Biol* **345**, 1157–1169.
25 Mehtälä ML, Haataja TJ, Blanchet CE, Hiltunen JK, Svergun DI & Glumoff T (2013) Quaternary structure of human, *Drosophila melanogaster* and *Caenorhabditis elegans* MFE-2 in solution from synchrotron small-angle X-ray scattering. *FEBS Lett* **587**, 305–310.
26 Hamed RB, Henry L, Gomez-Castellanos JR, Mecinovic J, Ducho C, Sorensen JL, Claridge TD & Schofield CJ (2012) Crotonase catalysis enables flexible production of functionalized prolines and carbapenams. *J Am Chem Soc* **134**, 471–479.
27 Hamed RB, Henry L, Gomez-Castellanos JR, Asghar A, Brem J, Claridge TD & Schofield CJ (2013) Stereoselective preparation of lipidated carboxymethyl-proline/pipecolic acid derivatives via coupling of engineered crotonases with an alkylmalonyl-CoA synthetase. *Org Biomol Chem* **11**, 8191–8196.
28 Hamed RB, Mecinovic J, Ducho C, Claridge TD & Schofield CJ (2010) Carboxymethylproline synthase catalysed syntheses of functionalised N-heterocycles. *Chem Commun (Camb)* **46**, 1413–1415.
29 Van Aalten DM, Milne KG, Zou JY, Kleywegt GJ, Bergfors T, Ferguson MA, Knudsen J & Jones TA (2001) Binding site differences revealed by crystal structures of *Plasmodium falciparum* and bovine acyl-CoA binding protein. *J Mol Biol* **309**, 181–192.
30 Kragelund BB, Andersen KV, Madsen JC, Knudsen J & Poulsen FM (1993) Three-dimensional structure of the complex between acyl-coenzyme A binding protein and palmitoyl-coenzyme A. *J Mol Biol* **230**, 1260–1277.
31 Hofstein HA, Feng Y, Anderson VE & Tonge PJ (1999) Role of glutamate 144 and glutamate 164 in the catalytic mechanism of enoyl-CoA hydratase. *Biochemistry* **38**, 9508–9516.
32 Wakil SJ (1956) Studies on the fatty acid oxidizing system of animal tissues. IX. Stereospecificity of unsaturated acyl CoA hydrase. *Biochim Biophys Acta* **19**, 497–504.
33 Rasmussen JT, Borchers T & Knudsen J (1990) Comparison of the binding affinities of acyl-CoA-binding protein and fatty-acid-binding protein for long-chain acyl-CoA esters. *Biochem J* **265**, 849–855.
34 Haataja TJ, Koski MK, Hiltunen JK & Glumoff T (2011) Peroxisomal multifunctional enzyme type 2 from the fruitfly: dehydrogenase and hydratase act as separate entities, as revealed by structure and kinetics. *Biochem J* **435**, 771–781.
35 Ellman GL (1959) Tissue sulfhydryl groups. *Arch Biochem Biophys* **82**, 70–77.
36 Petoukhov MV, Franke D, Shkumatov AV, Tria G, Kikhney AG, Gajda M, Gorba C, Mertens HDT, Konarev PV & Svergun DI (2012) New developments in the ATSAS program package for small-angle scattering data analysis. *J Appl Crystallogr* **45**, 342–350.
37 Svergun DI (1992) Determination of the regularization parameter in indirect-transform methods using perceptual criteria. *J Appl Crystallogr* **25**, 495–503.

38 Franke D & Svergun DI (2009) DAMMIF, a program for rapid ab-initio shape determination in small-angle scattering. *J Appl Crystallogr* **42**, 342–346.
39 Svergun DI, Petoukhov MV & Koch MHJ (2001) Determination of domain structure of proteins from X-ray solution scattering. *Biophys J* **80**, 2946–2953.
40 Petoukhov MV & Svergun DI (2005) Global rigid body modeling of macromolecular complexes against small-angle scattering data. *Biophys J* **89**, 1237–1250.
41 Kozin MB & Svergun DI (2001) Automated matching of high- and low-resolution structural models. *J Appl Crystallogr* **34**, 33–41.
42 Svergun D, Barberato C & Koch MHJ (1995) CRYSOL – a program to evaluate X-ray solution scattering of biological macromolecules from atomic coordinates. *J Appl Crystallogr* **28**, 768–773.
43 Kabsch W (2010) XDS. *Acta Crystallogr D* **66**, 125–132.
44 Evans PR & Murshudov GN (2013) How good are my data and what is the resolution? *Acta Crystallogr D* **69**, 1204–1214.
45 Collaborative Computational Project Number 4 (1994) The CCP4 suite: programs for protein crystallography. *Acta Crystallogr D* **50**, 760–763.
46 McCoy AJ, Grosse-Kunstleve RW, Adams PD, Winn MD, Storoni LC & Read RJ (2007) Phaser crystallographic software. *J Appl Crystallogr* **40**, 658–674.
47 Murshudov GN, Skubak P, Lebedev AA, Pannu NS, Steiner RA, Nicholls RA, Winn MD, Long F & Vagin AA (2011) REFMAC5 for the refinement of macromolecular crystal structures. *Acta Crystallogr D* **67**, 355–367.
48 Emsley P & Cowtan K (2004) Coot: model-building tools for molecular graphics. *Acta Crystallogr D* **60**, 2126–2132.
49 Chen VB, Arendall WB III, Headd JJ, Keedy DA, Immormino RM, Kapral GJ, Murray LW, Richardson JS & Richardson DC (2010) MolProbity: all-atom structure validation for macromolecular crystallography. *Acta Crystallogr D* **66**, 12–21.
50 Modis Y, Filppula SA, Novikov DK, Norledge B, Hiltunen JK & Wierenga RK (1998) The crystal structure of dienoyl-CoA isomerase at 1.5 Å resolution reveals the importance of aspartate and glutamate side chains for catalysis. *Structure* **6**, 957–970.
51 Larkin MA, Blackshields G, Brown NP, Chenna R, McGettigan PA, McWilliam H, Valentin F, Wallace IM, Wilm A, Lopez R *et al*. (2007) Clustal W and Clustal X version 2.0. *Bioinformatics* **23**, 2947–2948.
52 Krissinel E & Henrick K (2004) Secondary-structure matching (SSM), a new tool for fast protein structure alignment in three dimensions. *Acta Crystallogr D* **60**, 2256–2268.
53 Kabsch W & Sander C (1983) Dictionary of protein secondary structure: pattern recognition of hydrogen-bonded and geometrical features. *Biopolymers* **22**, 2577–2637.
54 Tamura K, Peterson D, Peterson N, Stecher G, Nei M & Kumar S (2011) MEGA5: molecular evolutionary genetics analysis using maximum likelihood, evolutionary distance, and maximum parsimony methods. *Mol Biol Evol* **28**, 2731–2739.
55 Mylonas E & Svergun DI (2007) Accuracy of molecular mass determination of proteins in solution by small-angle X-ray scattering. *J Appl Crystallogr* **40**, s245–s249.